IEEE Access
Multidisciplinary | Rapid Review | Open Access Journal

Received 25 March 2024, accepted 14 May 2024, date of publication 23 May 2024, date of current version 3 June 2024.

Digital Object Identifier 10.1109/ACCESS.2024.3404473

RESEARCH ARTICLE

Deep Learning Based Energy, Spectrum, and SINR-Margin Tradeoff Enabled Resource Allocation Strategies for 6G

VIVEK PATHAK[1], R. CHETHAN[2], RAHUL JASHVANTBHAI PANDYA[1], (Senior Member, IEEE), SRIDHAR IYER[3], (Senior Member, IEEE), AND VIMAL BHATIA[4,5,6], (Senior Member, IEEE)

[1]Indian Institute of Technology Dharwad, Karnataka, Dharwad 580011, India
[2]Indian Institute of Technology Kanpur, Uttar Pradesh, Kanpur 208016, India
[3]Department of Electronics and Communication, KLE Technological University Dr. MSSCET, Karnataka, Belagavi 590008, India
[4]School of Electronic and Information Engineering, Soochow University, Suzhou 215006, China
[5]Indian Institute of Technology Indore, Madhya Pradesh, Indore 453552, India
[6]Faculty of Informatics and Management, University of Hradec Kralove, 50003 Hradec Kralove, Czech Republic

Corresponding author: Vimal Bhatia (vbhatia@iiti.ac.in)

This work was supported in part by the Science and Engineering Research Board (SERB) Project EEQ/2020/000047 and Project SIR/2022/00095; in part by the University of Hradec Kralove, Faculty of Informatics and Management, Czech Republic Agency of Excellence, under Grant 2204/2023; in part by the International Institute of Information Technology, Bangalore, Communications Enterprise Technologies (IIITB COMET) Foundation, established under the Advanced Communication Systems Vertical of the National Mission on Interdisciplinary Cyber-Physical Systems (NM-ICPS), Department of Science and Technology, Government of India, Chair Professorship from Driving Innovation through Simulation Hub for Technologies in Interdisciplinary Cyber-Physical Systems (DRISHTI CPS), Ministry of Education, Scheme for Promotion of Academic and Research Collaboration (MoE SPARC) Project SPARC/2019-2020/P2264/SL; and in part by Soochow University, China.

ABSTRACT In the rapidly evolving landscape of wireless communication systems, the forthcoming sixth-generation technology aims to achieve remarkable milestones, including ultra-high data rates and improved Spectrum Efficiency (SE), Energy Efficiency (EE), and quality of service. However, a key challenge lies in the transmission at Terahertz frequencies, which entails significant signal loss, resulting in reduced signal-to-interference and noise ratio margins (Γ). Increased transmit power can ameliorate Γ and SE, thereby sacrificing EE. Consequently, it necessitates strategic Resource Allocation (RA) to uphold an optimal trade-off amid SE, EE and Γ. In this paper, we propose a series of RA strategic algorithms harnessing the Transfer Learning, Growth-Share (GS) matrix, Game Theory (GT), and service priorities to tailor the aforementioned trade-off. This endeavour renders the network more intelligent, self-sufficient, and resilient. Furthermore, we have seamlessly integrated Device-to-Device communication scenarios into our proposed algorithms, enhancing SE and network capacity. The proposed integration aims to strengthen overall system performance and accommodate the evolving demands of future wireless networks. Our primary contribution lies in the development of the GS-GT-based Optimal PathFinder (GS-GTOPF) algorithm to identify optimal paths based on SE using Deep Neural Networks. Thereafter, we formulate an enhanced version of it by integrating service priorities (GS-GTOPF-SP). This refinement has been further advanced by reducing the Computational Time (CT), resulting in GS-GTOPF-SP-rCT. Further improvement is achieved by introducing the angle criterion (GS-GTOPF-SP-rCT-θ). Extensive simulations demonstrate that angle criterion integrated algorithm, showcases a remarkable 76.12% reduction in CT while maintaining an accuracy surpassing 95% compared to GS-GTOPF. Moreover, prioritizing high-priority services leads to a significant enhancement of 12.97% and 62.95% in SE, 16.14% and 81.97% in EE, and 12.27% and 25.95% in Γ when compared to medium and low-priority services.

INDEX TERMS Terahertz (THz) communication, transferred learning (TL), energy efficiency (EE), spectrum efficiency (SE), signal to interference and noise ratio-margin (Γ), residual battery indicator (RBI).

The associate editor coordinating the review of this manuscript and approving it for publication was Hayder Al-Hraishawi.

I. INTRODUCTION

The continuous progression of wireless communication technology's advanced applications and use cases has led to a remarkable surge in the user demand for high Bandwidth (BW) and capacity. This trend has catalyzed a significant evolution in wireless technology, transitioning from the established fourth-generation (4G) networks to the impending 5G networks. While 4G is primarily aimed at interconnecting users, 5G is poised to interconnect things propelled by advancements in the Internet of Things (IoT).

The ongoing global deployment of 5G wireless networks promises to redefine how we connect and communicate [1]. Alongside this transformation, the potential impact of Artificial Intelligence/Machine Learning (AI/ML) in 5G networks is significant, with projections envisioning enhanced adaptability, efficiency, and intelligence. However, the extensive integration of AI/ML is in a nascent stage which presents an array of formidable challenges yet to be surmounted. On the other hand, the 6G wireless networks aspire for a complete ML/Deep Learning (DL) integration [2], [3], [4], [5], [6]. Consequently, 6G enables dynamic adjustments, resource optimization, fault prediction, enhanced security, and self-optimization, promising to revolutionize the networks into more responsive and intelligent communication infrastructures. Furthermore, 6G aims to effectuate unprecedented objectives, such as ultra-high data rates, enriched network capacity, Spectrum Efficiency (SE), Energy Efficiency (EE), Quality of Service and Experience (QoSE), system throughput, connectivity density, ultra-low latency, increased mobility, and reliability [7].

Further, 6G is poised to revolutionize connectivity, boasting speeds of up to 1 Tbps and an astonishingly low latency of 0.1 ms. This leap forward in technology will reshape industries in profound manners. Real-time virtual reality and augmented reality experiences will become seamless and immersive, paving the way for advanced gaming and remote collaboration. Besides, autonomous vehicles will benefit from high-speed connectivity, ensuring safer and more efficient driving experiences with instant responses to changing road conditions [8]. In healthcare, telemedicine will thrive with the ability to transmit high-definition medical data in real-time, facilitating remote consultations and surgeries. Smart cities and IoT infrastructures will be powered by 6G, enabling seamless communication between countless devices and real-time data analysis for optimizing resource usage and enhancing public safety [9]. Additionally, edge computing will undergo a boost, bringing computing power closer to end-users for faster processing of data-intensive applications like AI, ML, and IoT analytics. In essence, 6G's unparalleled performance will catalyze innovation and connectivity across industries, unlocking new levels of efficiency and possibilities previously unimaginable.

Moreover, these advanced use cases and the evolution of 6G technology necessitate a reassessment of performance metrics to effectively gauge the system's capabilities. Initial vision studies for 6G identified fundamental metrics, including peak- and user-experienced data rates, latency, reliability, coverage, connection density, SE, EE, and cost-efficiency. However, as research progresses, area traffic capacity, security capacity, mobility, and intelligence level are emerging as additional critical metrics for comprehensive performance evaluation [10]. Further, industries deeply engaged in 6G research emphasize specific metrics tailored to their needs, such as precise indoor and outdoor positioning accuracy, Quality of Perception and Experience (QoPE), and stringent reliability standards [11], [12]. As the deployment of 6G technology draws nearer, the continual introduction of new metrics is anticipated to be essential in accurately assessing the system performance and meeting the diverse requirements of advanced use cases.

As it is evident that in 6G, Terahertz (THz) frequencies (0.1–10 THz) are being viewed as a potential band for

TABLE 1. Comprehensive glossary of acronyms and symbols.

Acronym / Symbol	Interpretation
SE	Spectrum Efficiency
EE	Energy Efficiency
SINR	Signal-to-Interference and Noise Ratio
Γ	SINR-margin
DL	Deep-Learning
TL	Transfer-Learning
D2D	Device-to-Device
GS matrix	Growth-Share matrix
GT	Game Theory
GS-GTOPF	GS-GT-based Optimal PathFinder
GS-GTOPF-SP	GS-GT-based Optimal PathFinder with Service Priorities
GS-GTOPF-SP-rCT	GS-GTOPF-SP with reduced Computational Time
GS-GTOPF-SP-rCT-θ	GS-GTOPF-SP-rCT with Angle Criterion
RBI	Residual Battery Indicator
NSA	Normalized Spectrum Availability
β_n	RBI on n^{th} node
p_n	Transmitting power of n^{th} node
ν	NSA of the network
$h_{i,n}$	Channel gain between the i^{th} and j^{th} node
$\mathbf{H}$	Channel Matrix
SINR_n^k	SINR of the n^{th} node on the k^{th} path
γ_n^k	SINR-margin of the n^{th} node on the k^{th} path
SE_k	Spectrum Efficiency of the k^{th} path
EE_k	Energy Efficiency of the k^{th} path
$\sigma_{x,y}$	Transfer learning correlation factor
$\mathcal{R}$	Set of RBIs of all the nodes
$\mathcal{A}$	Set of active nodes
$\mathcal{I}$	Set of active nodes available for communication
$\mathcal{U}$	Set of all nodes from source (s) to destination (d)
$\mathcal{K}$	Set of all the possible paths from s to d
$\lambda_{s,d}^g$	Service requests between any pair (s,d) with priority levels $g = 1, 2,$ and 3 indicate Q1, Q2, and Q3 services respectively
$\mathcal{K}_i^\beta$	Average RBI levels of all the nodes in the i^{th} path in set $\mathcal{K}$
γ_{avg}^i	Average SINR-margins of all the nodes in the i^{th} path in set $\mathcal{K}$
ρ_x^g	Indicates the priority allocation x for service g
$\mathcal{SE}$	Set of SE of all the paths
$\lvert\mathcal{K}_i\rvert$	Hop-count of i^{th} path in set $\mathcal{K}$
$w_{i,j}$	Width of the link between the i^{th} and j^{th} node
$\overline{w}_i^h$	Width of the widest path from the source node to any other i^{th} node such that the path has at most h hops
$\lvert\widehat{\mathcal{K}}_j^h\rvert$	Hop-count of the widest path from the source node to i^{th} node such that the path has at most h hops
$\vec{d}_{s,i}$	Distance vector from the source node to i^{th} node
θ_i	Angle between the source node and i^{th} node

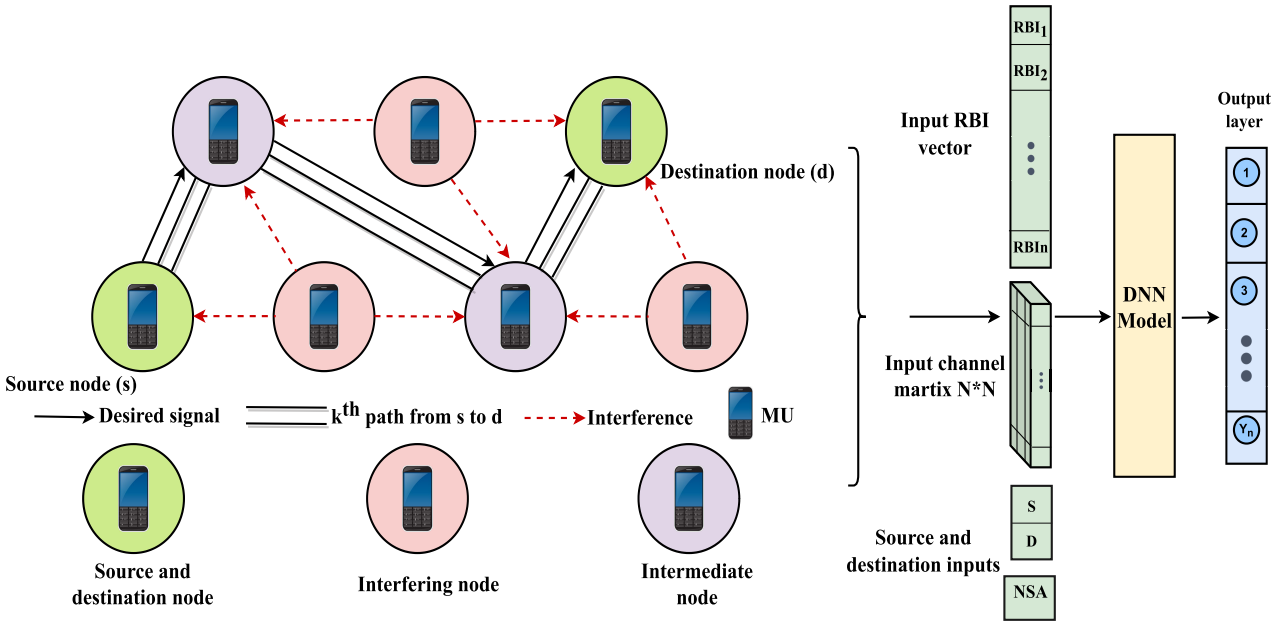

FIGURE 1. DL integrated multi-hop communication depicting desired signal and interference on the k^{th} path between source and destination nodes.

communication; however, operating at THz frequencies incurs immense path losses, atmospheric absorption, rain attenuation, scattering, penetration losses, and human blockage, resulting in a lower Signal-to-Interference and Noise Ratio (SINR) [7], [13]. As a result, there will occur a trade-off between SE, EE, and system performance, i.e., to proliferate EE, SE is sacrificed, and vice versa [14], [15], [16], [17], [18], [19]. To address this trade-off, within our innovative framework designed to augment network efficiency, we have integrated Device-to-Device (D2D) communication, which accomplishes direct data exchange among proximate mobile devices. In this scenario, devices within proximity can establish direct communication, circumventing the traditional cellular network infrastructure. This approach yields numerous benefits, including lower latency, increased SE, EE, and augmented network capacity. In our investigation, we have devised an optimal path finder algorithm modelled for D2D communication scenarios. This algorithm facilitates efficient and reliable communication among devices by identifying the most suitable optimal paths for direct data exchange, thereby optimizing resource utilization and increasing overall network performance. As highlighted before, in 6G, on the one hand, the communication devices will be operated in an energy-efficient manner to transmit with lower power; on the other hand, operation at THz frequencies will result in excessive losses. Hence, it is essential to ensure higher SINR-margins (Γ) for the larger reach, consequently leading to lower EE. Further, to achieve higher SE, spectrum allocation will be confined, which will reduce the Γ. These key aspects serve as the motivation to propose DL-based methodological strategies to address the trade-off between SE, EE, and Γ.

II. RELATED WORKS

The research community has focused on exploring the trade-offs between SE, EE, and system performance. T. S. Rappaport et al. provided a comprehensive survey on 6G-THz communication, discussing vision, drivers, technologies, opportunities, challenges, and open research problems [13]. They also introduced novel propagation and partition loss models for frequencies above 100 GHz, addressing signal degradation and adaptive beamforming to mitigate higher path losses [13]. W. Saad et al. outlined a futuristic vision for 6G, addressing technologies, challenges, research opportunities, primary drivers, target performance parameters, and proposed applications [3]. Their work presents a roadmap and motivation for innovative research in 6G.

However, many researchers demonstrate the importance of integrating AI, ML, and DL to automate the performance of 6G wireless networks, optimize SE, EE, system performance, SINR, reduce latency, and improve reliability and other performance metrics.

In particular, K. B. Letaief et al. proposed a potential technological roadmap and AI-enabled optimization methodologies coalesced with 6G wireless networks [5]. S. Fu et al. conferred AI-assisted intelligent architecture and edge computing-based joint Resource Allocation (RA) algorithm attaining superior performance and demonstrating reduced Computational Time (CT) and BW consumption [2]. T. Huang et al. presented a survey on unaccustomed architectural changes amalgamated with green 6G networks, AI-based enhanced networking protocols, and potential technologies forging seamless communication [22].

TABLE 2. A comparative summary of most related research work under consideration.

Ref. No.	Performance metrics optimization	Technology employed	Mode of communication	Model type	TL	GT
[14]	Joint optimization of SE and EE	AI/ML	D2D	DNN	✗	✗
[15]	Joint optimization of SE and EE	Fractional programming	Multioperator multiuser-MIMO	✗	✗	✗
[16]	Joint optimization of SE and EE	✗	D2D massive-MIMO	✗	✗	✗
[20]	EE	✗	Full-duplex transmission	✗	✗	✓
[21]	EE	✓	Intra-cluster node communication	NN	✗	✗
Proposed	**Joint optimization of SE and EE**	**DL**	**Multihop D2D communication**	**DNN**	✓	✓

M. Chen et al. presented a survey on modern conglomerate wireless networks, advanced learning systems equipping superior computing capacity, and rapid and profoundly intelligent learning algorithms based on flexible input mechanisms [23]. The study aims to enable researchers to develop further wireless networks based on Artificial Neural Networks (ANN).

Furthermore, the authors in [23], [24], [25], [26], [27], [28], [29], [30], [31], [32], [33], [34], [35], and [36] emphasized the importance of EE in 6G wireless communication, demonstrating the reduced energy cost and carbon footprint. Moreover, the authors in [23], [24], [25], [26], [27], [28], [29], [30], [31], [32], [33], [34], [35], and [36] illustrated green energy efficiency and Energy Harvesting (EH) frameworks, optimization methodologies and RA, routing protocols, and a Game Theory (GT) approach. In particular, P. Annamalai et al. introduced a RA algorithm accomplishing increased SE in 5G and beyond cellular networks [24]. S. K. M. M. Mowla et al. examined the novel energy-efficient model for 5G heterogeneous green networks exhibiting 48% power saving compared to the existing models [25]. J. Shi et al. proposed hybrid radio access optimization algorithms by blending the Non-Orthogonal Multiple Access and Orthogonal Frequency Division Multiplexing (OFDM), thereby enhancing the EE for the next-generation wireless systems [26]. D. Zhai et al. unveiled the energy-efficient RA employing OFDM for the D2D users and sparse code multiple access for cellular users in co-existing cellular networks [27]. F. Fang et al. formulated a non-convex RA problem for the joint optimization of subchannel and Power Allocation (PA) considering the co-channel and cross-tier interference, improving EE [28].

Considering dynamic spectrum sharing environments, K. Hamedani et al. introduced a novel energy-efficient spectrum sensing method employing advanced Recurrent Neural Networks (RNNs) for Multiple Inputs, Multiple Outputs (MIMO)-OFDM systems [29]. Y. Guo et al. demonstrated reduced complexity threshold-based pair switching methods for energy transfer in largescale SWIPT-enabled cellular networks [30]. J. Wu et al. offered a study of EH-aided latency and energy-efficient methods for wireless communication [31]. P. Yan et al. investigated the energy-aware relay selection method optimizing the trade-off between security and reliability by employing the EH cooperative and Cognitive Radio (CR) access systems [32]. M. Feng et al. investigated a problem of the Base Station (BS) on-off considering MIMO-heterogeneous networks, maximizing the EE employing the GT and equilibrium approaches [33]. X. Ge et al. proposed the algorithm based on the interference and EE models employing the leading field GT and the Nash equilibrium Hamilton-Jacobi–Bellman and Fokhar-Planck-Kolmogorov equations improving the EE and outage probability [20]. A. Shahid et al. proposed a self-organized optimization framework for allocating power levels and sub-channels by utilizing a non-cooperative game to maximize the EE and demonstrate higher performance [34].

Furthermore, AI/ML/DL integration is essential for enhanced EE in 6G wireless communication. In particular, B. Mao et al. offered an exhaustive survey enwrapping AI models to accomplish green communication for 6G [21]. P. Goswami et al. presented an AI-enabled energy-efficient routing protocol for the intelligent transport system [21]. Y. M. A. Qureshi et al. inferred the Reinforcement Learning (RL)-based contextual unimodal multi-arm bandits dynamic RA independent of any Channel State Information (CSI), improving the EH and EE [35]. I. Al Qerm et al. presented the energy-efficient conditional traffic offloading employing RL considering the traffic load on macro and a small BS such that the power consumption is minimized, preserving congestion and interference in control [36]. N. Hu et al. proposed an energy-efficient network computing paradigm for 6G, integrating network functions into a general computing platform instead of delegating computing tasks to network devices [37].

Alongside EE, optimizing SE is equally vital to preserve adequate QoS by imparting high-quality spectrum and granting fair user access to the network resources. However, traditionally, to improve EE, we sacrifice SE and vice versa; therefore, there is a trade-off between SE and EE. To identify the optimal trade-off between SE and EE, the authors in [7], [14], [15], [16], [37], [38], [39], [40], [41], and [42] focused on jointly optimizing SE and EE. In particular, O. Aydin et al. presented the optimization problem considering the trade-off between SE and EE and derived a pattern-optimized solution under the constraints of service level agreement [15]. A. He et al. introduced a flexible spatial dynamic power control scheme mitigating cellular-D2D interference to

optimize the SE and EE simultaneously [16]. In ultra-dense networks, C. Yang et al. conferred a trade-off study between SE and EE with a Nash bargaining-based cooperative GT approach accomplishing the maximal EE at a sub-optimal SE equilibrium employing the closed-form approximation. The authors engaged the mean-field method to characterize and mitigate the complex interference influence, attaining 30% of fairness and trade-off improvement compared to the conventional approach [38]. Q. V. Pham et al. investigated an optimization algorithm for RA, maintaining the trade-off between EE and SE in the presence of interference in 5G wireless networks [39]. C. He et al. present the ML-based energy-efficient PA by practicing the clustering method in a distributed antenna system, maximizing the SE and EE considering the interference [40]. M. Yan et al. presented the federated cooperation and augmentation for PA in decentralized wireless networks, demonstrating increased robustness, accurate PA, and remarkable convergence compared to the other benchmark algorithms [41]. M. Alnakhli et al. presented the optimization algorithm considering the injected traffic patterns D2D communication networks enhance the SE and EE through the optimized RA employing u-matrix theory [17]. H. Ngo et al. considered a cell-free MIMO downlink derived a closed-form expression for the SE, and designed an optimal PA algorithm to improve EE [42]. M. Sengly et al. studied the joint optimization of EH and SE in wireless D2D networks by applying a Deep Neural Network (DNN) learning algorithm [14]. M. Rahman et al. considered a subsidy-based spectrum-sharing market to facilitate co-primary spectrum sharing where providers are explicitly incentivized to share spectrum resources and introduced a game-theoretic model to regulate free-riding [43]. Moreover, Friedrich et al. conducted a measurement study using an indoor mesh testbed to analyze the multi-hop behaviour of the IEEE 802.11n standard with MIMO. The authors examined the throughput behaviour and its relationship with path length, maximum aggregate size, and channel bonding options for the IEEE 802.11n standard [44]. The study concluded that throughput decreases exponentially as the path length increases.

From the aforementioned detailed survey of recent related studies alongside most related research work under consideration, as illustrated in Table 2, it can be inferred that there is no existing study which has considered the hybrid approach of DNN, Transfer Learning (TL), GT, and Growth Share (GS) matrix-based integration for SE, EE, and Γ trade-off optimized RA, considering the Service Priorities (SP) in 6G wireless communication networks. Therefore, we are motivated to propose a DL-based RA methodology for 6G wireless networks, which addresses the SE, EE, and Γ trade-offs.

A. KEY CONTRIBUTION

This article proposes a DL-based RA methodology for 6G wireless networks, aiming to achieve optimal trade-off amid SE, EE, and Γ. To acclimatize the aforementioned trade-off, we propose novel RA strategies based on the Γ, such as aggressive, defensive, and moderate for THz in the 6G wireless communication networks. Moreover, we incorporate a D2D communication scenario into our proposed model to enhance overall network efficiency in terms of SE, EE, and Γ. It's evident as edge computing offloads AI algorithms to base stations, leveraging D2D communication to facilitate direct data exchange between nearby devices, bypassing the need for transmission through base stations. This approach reduces interference, maximizes spectrum utilization, and enhances Γ as D2D communication enables shorter transmission distances, resulting in stronger signal strengths and lower interference compared to traditional cellular transmissions. Furthermore, complete integration of the DL and TL model is exploited to optimize network efficiency, ensuring seamless blending of the mixed input DNN and TL in the proposed algorithms. The key contributions of this paper are outlined below:

1) Firstly, we propose an innovative algorithm which is GS matrix-GT-based Optimal PathFinder (GS-GTOPF), which integrates DNN and TL to proliferate EE and SE by leveraging Residual Battery Indicators (RBIs) and Γ values. The primary objective of this algorithm is to optimize the pathfinding process in D2D wireless networks, effectively balancing energy consumption and spectral utilization for improved performance.
2) We further enhance network performance by introducing a second algorithm, GS-GTOPF-SP, which extends the capabilities of GS-GTOPF by incorporating service priority-based node and path selection. This augmentation prioritizes high data rate services to reduce waiting times and optimize overall network efficiency.
3) Furthermore, we introduced a third algorithm, GS-GTOPF-SP-rCT, which builds upon GS-GTOPF-SP by integrating optimization techniques from [45]. This novel algorithm is modelled to refine GS-GTOPF-SP by identifying solutions with reduced CT, thus improving efficiency in network optimization processes.
4) Finally, we introduced a fourth algorithm, an extension of the third iteration, denoted as GS-GTOPF-SP-rCT-θ. This novel algorithm incorporates the angle criterion, significantly reducing CT, albeit with a minor compromise in accuracy.

To the best of the authors' knowledge, there exists no study which considers the hybrid approach of DNN, TL, GT, and GS matrix-based integration for SE, EE, and Γ trade-off optimized RA, considering service priorities in 6G wireless communication. The current study is the first to propose novel optimization RA strategies to identify the optimal trade-off amid SE, EE, and Γ, simultaneously employing DNN, GT, GS, and service priorities.

The rest of the article is organized as follows. Section II comprises all the existing related research under consideration. Section III comprehends the details of the proposed

system model. Section IV provides an extensive analysis of the proposed model. Section V details the simulation environment and provides a detailed analysis of the results. Lastly, Section VI concludes the overall study of the proposed article. Moreover, we have defined the most frequently used acronyms and symbols, along with their interpretations, throughout the paper, as illustrated in Table 1.

Notations: Matrices are represented by bold uppercase letters (e.g., $\mathbf{H}$), while bold lowercase letters denote vectors (e.g., α). Scalars are denoted in normal font (e.g., β). For any general matrix $\mathbf{H}$, $\mathbf{H}^H$, rank($\mathbf{H}$), and $\mathbf{H}_{i,j}$ denote its conjugate transpose, rank, and $(i,j)^{th}$ element, respectively. $\mathbf{I}$ and $\mathbf{0}$ signify an identity matrix and an all-zero matrix, respectively, with appropriate dimensions unless specified otherwise. Sets are denoted by calligraphic letters, e.g., $\mathcal{K}_i$ denotes the i^{th} element of the set $\mathcal{K}$. $|\mathcal{K}|$ denotes the total number of elements in the set. $\mathbb{C}^{x\times y}$ denotes the space of $x \times y$ complex-valued matrices. The notation $\mathcal{CN}(\mu, \sigma^2)$ indicates a circularly symmetric complex Gaussian distribution, $\sim$ stands for "distributed as", and | stands for "given that".

III. SYSTEM MODEL

This section presents the comprehensive system model considering an EH deployment, Power Transmission (PT), Path-Loss (PL) channel model, DL, and TL solution for the 6G and beyond communication networks. The communication system comprises Mobile User (MU) nodes with wireless power transfer and energy harvesting capabilities, using beamforming transceivers for MIMO configurations. Communication occurs via direct or D2D links through intermediate nodes, considering path loss and Rayleigh fading in the THz range. Fig. 1 illustrates a typical multi-hop D2D communication scenario for the k^{th} path from the source node to the destination node. It demonstrates the intended signal transmitted by the nodes along the path, as well as the interference experienced by the receiving nodes along the same path. Consequently, an optimal pathfinder algorithm ensures communication constraints with SINR-governed path selection. BW-sharing guarantees equal distribution; however, routing optimization faces challenges due to non-isotonic and non-monotonic metrics addressed by proposed efficient algorithms. EE considers power consumption and transmitted powers optimized using GS matrices. The setup optimizes SE and energy consumption while considering path loss, interference, and noise. Further details can be found in subsequent subsections.

A. EH, NODE DEPLOYMENT, AND PT MODEL

Each node is equipped with a RBI, on which the DL model, illustrated in Fig. 2, commissions the node's engagement in establishing the communication. Eq. (1)-(3) describes the EH, deployment, and PT models where $\beta_n \sim \mathcal{N}(\mu = 0.5, \sigma^2 = 0.1)$ is Gaussian distribution with mentioned parameter, representing nodes' RBI levels and $\delta^{RBI}(n)$ is a binary variable that controls the participation of the n^{th} node in the communication [46], [47]. Eq. (2) assigns the n^{th} node to participate in establishing the communication if $\beta_n \geq 0.3$ $(\mu - 2\sigma)$, else the node is configured for EH and is given by

$$\mathcal{R} = \{\beta_n, n = \{1, 2, \ldots, N\}\} \tag{1}$$

$$\delta^{RBI}(n) = \begin{cases} 0 \text{ (EH mode)} & \beta_n < 0.3 \\ 1 \text{ (Active mode)} & \beta_n \geq 0.3 \end{cases} \tag{2}$$

When the node configured in EH includes $\beta_n \geq 0.3$, the permission is granted for communication, demonstrating a satisfactory Γ. However, the node's battery level indicators indicate the status of a battery in terms of residual energy and time elapsed to drain or charge it. Moreover, to determine reach till which energy savings can be achieved without squandering it, the author in [46], [47] executed a real-world experiment on 4000 mobile users for four weeks and attempted to analyze the users' routine behaviour for battery consumption. Consequently, the experiment concluded that the most common battery consumption behaviour emerges when the battery level is above 30% (0.3). However, it is observed at 65% and 74%, respectively, around midnight and early morning, exhibiting a bell-shaped curve. Therefore, adopting an identical concept for a passive battery in wireless communication networks, however, RBI values are drawn from the Gaussian distribution. Now let the scenario specifically be in the THz communication range; these passive nodes need to be active for transmission, which acquires a battery level of $\geq$0.3 else remains in harvesting mode.

$$p_n = \begin{cases} 31.76\ dBm \text{ (Maximum Tx power)} : \beta_n \geq 0.5 \\ 12\ dBm \text{ (Curtailed Tx power)} : 0.3 \leq \beta_n < 0.5 \end{cases} \tag{3}$$

$$\nu = \frac{\text{Complete spectrum} - \text{Occupied spectrum}}{\text{Complete spectrum}} \tag{4}$$

Eq. (3) formulates the PT model under the constraint that if $\delta^{RBI}(n) = 1$, the node is deployed in establishing the communication. Participating nodes transmit curtailed powers entrenched from GT, described in the subsequent sections. p_n indicates the transmitted power at n^{th} node, up to 31.76 dBm ($\beta_n \geq 0.5$) and limited to 12 dBm ($0.3 \leq \beta_n < 0.5$) [46], [47]. Moreover, Eq. (4) indicates the Normalized Spectrum Availability (NSA), denoted as ν, as shown above.

B. PL MODEL

In this subsection, we describe the PL model considering THz frequencies [13], which is shown by Eq. (5), as employed in the current study. The proposed DL model configures the paths with transitional nodes satisfying the $\beta_n \geq 0.3$, compensating the end-to-end PL accomplishing an acceptable Γ (aggressive, defensive, or moderate). Eq. (6) represents the Free Space Path Loss (FSPL), whereas Eq. (7) represents the total attenuation $\alpha[dB]$ experienced by the signal as a consequence of atmospheric absorption and

penetration losses as shown below [13].

$$\mathrm{PL}(f,d)[dB] = \mathrm{FSPL}(f,d)[dB] + \alpha[dB] + N_p[dB] + \chi_{shd}[dB] \quad (5)$$

$$\mathrm{FSPL}(f,d)[dB] = 20\log_{10}\left[\frac{4\pi fd}{c}\right] \quad (6)$$

$$\alpha[dB] = \eta(dB/m)\cdot d(m) + \Pi(dB/cm)\cdot\xi(cm) \quad (7)$$

Here, $\mathrm{PL}(f,d)[dB]$, f, d, and c, indicate the composite PL, THz frequency, the distance between source and destination, and velocity of light in the vacuum, respectively. $N_p[dB]$ specifies the noise penalty imposed by the Gaussian noise with distribution $\mathcal{N}(0,\sigma^2)$, with zero mean and standard deviation of σ. $\chi_{shd}[dB]$ indicates the penalty accounted for the human shadowing effect, $\eta(dB/m)$ implies the atmospheric attenuation coefficient when the carrier frequency is in the range of 100 GHz to 10 THz, $d(m)$ denotes the distance between source and destination, $\Pi(dB/cm)$ indicates the thickness attenuation coefficient of the partition material, and $\xi(cm)$ indicates the thickness of the partition material.

C. COMMUNICATION SYSTEM AND CHANNEL MODEL

The communication system comprises N MU nodes endowed with wireless power transfer and EH capability. Each MU node is implemented with M beamforming transceivers, enabling various MIMO configurations. Any source-destination (s,d) pair is permitted to establish a direct or D2D communication via intermediate nodes. We highlight here that the communication scenario and parameters considered in the current study are general. As a result, data exchange between the end devices is facilitated through a novel optimal pathfinder algorithm for RA, accompanying all pertinent communication constraints, which are discussed in detail in the subsequent subsections. Next, we detail the considered scenario and the related parameters.

The communication channel is established by intriguing a THz frequency considering the antecedent PL formulated in Eq. (5) and Rayleigh fading.

$$\mathrm{SINR}_n^k = \frac{p_{n-1}^k |h_{(n-1),n}|^2}{\sum_{i\in N\setminus\{n-1,n\}} p_i |h_{i,n}|^2 + \sigma^2} \quad \forall n \in k, \forall k \in \mathcal{K} \quad (8)$$

Moreover, Eq. (8) computes the SINR of the n^{th} node on the k^{th} path amid any (s,d) pair, with set $\mathcal{K}$ containing possible paths for any (s,d) pair, p_{n-1}^k is the power transmitted by the $(n-1)^{th}$ to n^{th} node, $|h_{(n-1),n}|^2$ is the magnitude of signal attenuation from the $(n-1)^{th}$ to the n^{th} node, $\sum_{i\in N\setminus\{n-1,n\}} p_i |h_{i,n}|^2$ evinces interference incurred at the n^{th} originated from the rest nodes, and σ^2 indicates the Additive White Gaussian Noise (AWGN) power.

$$\gamma_n^k = (SINR_n^k) - (min\text{-}SINR_n^k) \quad (9)$$

$$\gamma_n^k = \frac{[p_{n-1}^k - p_n^{min}]|h_{(n-1),n}|^2}{\sum_{i\in N\setminus\{n-1,n\}} p_i |h_{i,n}|^2 + \sigma^2} \quad \forall n \in k, \forall k \in \mathcal{K} \quad (10)$$

Further, Eq. (9)-(10) enumerate $\boldsymbol{\gamma}_n^k$, measuring additional received SINR_n^k over the minimum threshold (min-SINR_n^k) on k^{th} path and n^{th} node, where p_n^{min} is minimum power required at the n^{th} receiving node accomplishing minimum min-SINR^k, considered as a threshold for error-free detection. For a given path k, $\mathbf{l}^k$ denotes the vector of nodes on the k^{th} path, and $|\mathbf{l}^k|$ intermediate links, amid any (s,d) pair, considering the equal BW sharing constraint [48], Eq. 12 discovers the optimal path with maximized SE_k as shown below,

$$SE_k = \left\{\frac{\log_2(1+\min_{n\in\mathbf{l}^k}(\mathrm{SINR}_n^k))}{|\mathbf{l}^k|}\right\} \quad (11)$$

$$SE_k^{opt} = \max_{k\in\mathcal{K}}[SE_k] \quad (12)$$

The authors in [48] and [49] conferred that the Bellman-Ford's or Dijkstra's shortest path algorithms cannot be employed to solve Eq. 12 because the routing metric is neither isotonic nor monotonic. Consequently, Eq. 12 is solved by an exhaustive search method exploring all possible paths for a given (s,d) pair, resulting in increased CT. On the other hand, the exponential rise in CT makes exhaustive search prohibitive in dense networks. However, the authors in [45] presented efficient algorithms, obtaining optimal solutions to Eq. 12 in polynomial-time, which is embedded in our work.

$$EE_k = \frac{SE_k}{\sum_{i=1}^{N}(p_n^k + p_{ckt})} \quad \forall k \in \mathcal{K} \quad (13)$$

Furthermore, the Eq. 13 computes the EE for a path k between (s,d) as indicated by EE_k, in bits/joule/hertz. Where p_n^k is the transmitted power at the n^{th} intermediate node over k^{th} path and p_{ckt} indicates static power consumed in the circuit elements during the transmission. The transmitted powers are determined using the GS-matrix [50], as presented above.

D. PROBLEM FORMULATION AND ITS SOLUTION

In the aforementioned scenario, we have formulated an optimization problem, which is a weighted summation of SE and EE considering the weight parameters denoted as λ_{SE} and λ_{EE}, respectively. Moreover, the channel matrix $\mathbf{H}$ holds the channel gains from each node to every other node. Our objective is to jointly maximize SE and EE, accounting for constraints that ensure the attainment of desired Γ. Here, SINR_{th} signifies the difference between lower and upper SINR thresholds, $[(\mathrm{SINR})_{th\text{-}1} - (\mathrm{SINR})_{th\text{-}2}]$, as stipulated by the constraint articulated in Eq.14. Whereas the $(\beta)_{th}$ and v_{th} are the threshold battery level indicator and available threshold frequency check, determining the moment at which a node engages in transmission. Subsequently, the optimization problem is formulated and solved accordingly, elucidated herein below.

$$.Y(\mathbf{H}) = \max_{k\in\mathcal{K}}[\lambda_{SE}\ SE_k + \lambda_{EE}\ EE_k] \quad \forall k \in \mathcal{K}$$

$$s.t. = \begin{cases} \lambda_{SE}, \lambda_{EE} > 0 \\ \beta_n \geq (\beta)_{th} \\ \nu \geq \nu_{th} \\ \gamma_n^k \geq (\text{SINR})_{th} \\ (\text{SINR})_{th} \in [(\text{SINR})_{th\text{-}1} - (\text{SINR})_{th\text{-}2}] \end{cases} \tag{14}$$

Substituting the value of SE and EE from Eq. 11 and 13 into Eq. 14 gives

$$Y(\mathbf{H}) = \max_{k \in \mathcal{K}} \left[\lambda_{SE} \left(\frac{\log_2(1 + \min_{n \in L_k}(\text{SINR}_n^k))}{|\mathbf{l}^k|} \right) + \lambda_{EE} \left(\frac{SE_k}{\sum_{i=1}^{N}(P_n^k + P_{ckt})} \right) \right] \forall n \in k, \forall k \in \mathcal{K}$$
$$s.t. \text{ of Eq.14} \tag{15}$$

Applying the Lagrangian multiplier method which yields the following equation as mentioned below.

$$\mathcal{L}_g(\mathbf{H}, \psi, \omega, f, \lambda_1, \lambda_2, \lambda_3) = Y(\mathbf{H}) + \lambda_1[(\beta)_{th}(\psi, \omega) - \beta_n(\psi, \omega)] + \lambda_2[\nu_{th} - \nu(f)] + \lambda_3[(\gamma_n^k(\mathbf{H}))_{th} - \gamma_n^k(\mathbf{H})] \tag{16}$$

here $\mathcal{L}_g$ is a Lagrangian function and $\lambda_1, \lambda_2, \lambda_3$ are the Lagrangian multipliers. From Eq. 16, the gradient will be calculated as follows.

$$\Delta_{(\mathbf{H},\psi,\omega,f,\lambda_1,\lambda_2,\lambda_3)}\mathcal{L}_g(\mathbf{H}, \psi, \omega, f, \lambda_1, \lambda_2, \lambda_3) = \left(\frac{\partial \mathcal{L}_g}{\partial \mathbf{H}}, \frac{\partial \mathcal{L}_g}{\partial \psi}, \frac{\partial \mathcal{L}_g}{\partial \omega}, \frac{\partial \mathcal{L}_g}{\partial f}, \frac{\partial \mathcal{L}_g}{\partial \lambda_1}, \frac{\partial \mathcal{L}_g}{\partial \lambda_2}, \frac{\partial \mathcal{L}_g}{\lambda_3} \right) \tag{17}$$

here, $Y(\mathbf{H})$ is an optimization problem which is a function of channel matrix $\mathbf{H}$, β_n of battery is a function of ψ and ω, where ψ is hours of the day and ω is battery percentage which is a Gaussian distributed behaviour of a battery enabled node having a life-time of limited span. $\nu(f)$ is a function of available frequency f. Furthermore, Eq. 15 is an optimization problem that infers to finding the best path between the source and the destination by solving the optimal solution of it, which acquires a limited number of constraints, such as $\beta_n(\psi, \omega)$, $\nu(f)$ and $\gamma_n^k(\mathbf{H})$. Further, to find the optimal solution to the above-stated optimization problem, the gradient of the Lagrangian is evaluated as follows.

$$\Delta_{(\mathbf{H},\psi,\omega,f,\lambda_1,\lambda_2,\lambda_3)}\mathcal{L}_g(\mathbf{H}, \psi, \omega, f, \lambda_1, \lambda_2, \lambda_3) = 0 \tag{18}$$

$$\frac{\partial \mathcal{L}_g}{\partial \mathbf{H}} = 0 \tag{19}$$

$$\Rightarrow \frac{\partial[Y(\mathbf{H}) + \lambda_3\{(\gamma_n^k(\mathbf{H})_{th}) - (\gamma_n^k(\mathbf{H}))\}]}{\partial \mathbf{H}} \tag{20}$$

$$\frac{\partial \mathcal{L}_g}{\partial \psi} = 0 \Rightarrow \frac{\partial[\lambda_1\{\beta_{th}(\psi, \omega) - \beta_n(\psi, \omega)\}]}{\partial \psi} \tag{21}$$

$$\frac{\partial \mathcal{L}_g}{\partial \omega} = 0 \Rightarrow \frac{\partial[\lambda_1\{\beta_{th}(\psi, \omega) - \beta_n(\psi, \omega)\}]}{\partial \omega} \tag{22}$$

$$\frac{\partial \mathcal{L}_g}{\partial f} = 0 \Rightarrow \frac{\partial[\lambda_2\{\nu_{th} - \nu(f)\}]}{\partial f} \tag{23}$$

$$\frac{\partial \mathcal{L}_g}{\partial \lambda_1} = 0 \Rightarrow [\beta_{th}(\psi, \omega) - \beta_n(\psi, \omega)] \tag{24}$$

$$\frac{\partial \mathcal{L}_g}{\partial \lambda_2} = 0 \Rightarrow [\nu_{th} - \nu(f)] \tag{25}$$

$$\frac{\partial \mathcal{L}_g}{\partial \lambda_3} = 0 \Rightarrow [(\gamma_n^k(\mathbf{H})_{th}) - (\gamma_n^k(\mathbf{H}))] \tag{26}$$

Consequently, by solving Eq. 19-26, we achieve the optimal trade-off between SE, EE, and Γ. We implemented a DNN model to optimize SE while ensuring a minimum EE. Additionally, we created a dataset by solving Eq. 15, which jointly optimizes SE and EE. Subsequently, through the multiple iterations, the data generated is fed to the DL model, which we have analyzed in the subsequent sections.

E. DNN MODEL

Fig. 2 renders the multi-input DNN model consisting of four distinct input branches. The data sample input to the DNN is combined from the input parameters, such as RBI vector (N × 1), channel matrix (N × N), (s, d) pair (2 × 1), and ν (1 × 1), which is used to compute the SE and identify an efficient path (Y_n × 1) for each (s, d) pair. Each input branch contains a 'F' Fully Connected (FC) hidden layers in the Neural Network (NN). At the input of each branch, batch normalization is performed; each branch produces a vector; the output of all branches except the channel matrix branch are vectors. Furthermore, the channel matrix branch's output is flattened into a vector {(N × N) × 1} when interlacing with FC hidden layers of the NN. Each branch learns from the respective input parameter and contributes to predicting the optimal path, and the information acquired by all branches is combined in the concatenated layer. The concatenated layer consolidates the learned information from each branch, which is transferred to FC hidden layers to further learn from the collective knowledge and discover the optimal path. The output vector (Y_n × 1) facilitates the optimal path between a given (s, d) pair, ensuring the trade-off between SE, EE, and Γ.

The presented model employs the Adam optimizer and backpropagation, Rectified Linear Unit (ReLU), configuring a learning rate of 0.001, and evaluated training loss in Mean Square Error (MSE). Here, A_n indicates the number of neurons in the hidden layer of the RBI input branch is 30, and the shape of the hidden layer in channel matrix input $N \times C_n$ is 30 × 80. Moreover, the second branch of the DNN model is intended to learn the channel matrix. However, the initial stage of the N×N channel matrix is subject to batch normalization. The output of this stage will also be 30 × 30 input samples fed to a 2-D dense hidden layer with N=30 rows and N=80 columns, respectively, which consequently acts as the general matrix multiplication of a 30 × 30 input. Therefore, the output of this dense layer will be a 30 × 80 matrix. Furthermore, the depth of input layers in the (s, d) and NSA input branches are S_n and D_n, which are 10 and 20, respectively. Each input branch is F layers broad, where F is 3. The final FC layers are T_n neurons deep and F'

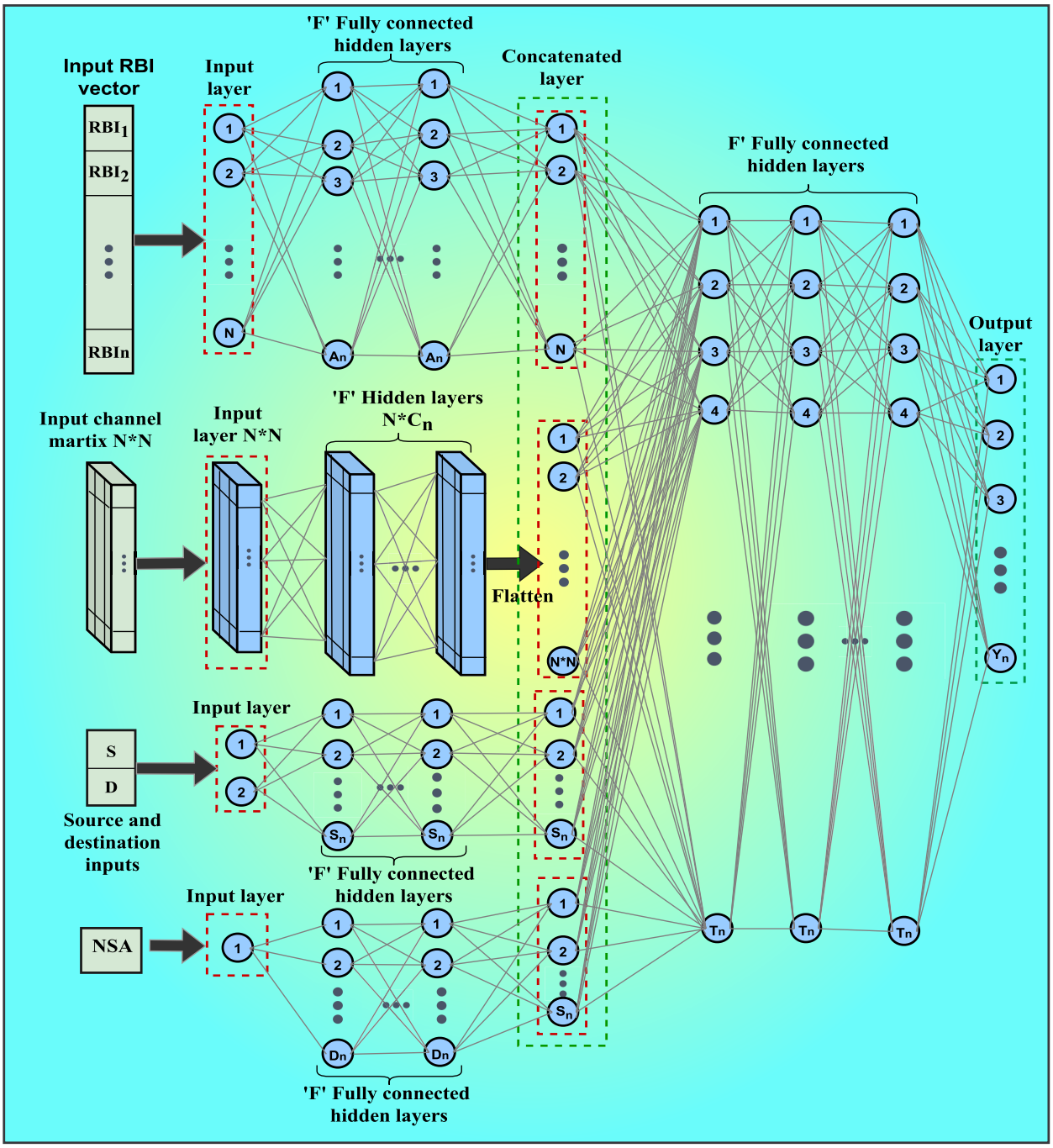

FIGURE 2. An illustration of a multi-input DNN model incorporating mixed data inputs and providing path output.

layers broad where T_n is 100, and F' is 3. The output layer has $'Y'_n$, i.e., 6 neurons.

F. TL MODEL

TL is a sub-branch of DL in which the NN learns from the source (x) domain amid the pre-training phase, executes the Fine-Tuning (FT), and administers the knowledge to the target (y) domain [51]. As illustrated in Fig. 3, during the RA in the (x) domain, the respective DL agent is trained, and the (x) domain's learning is transferred to the (y) domain. The (y) domain's DL agent adopts the transferred state and fine-tunes by performing backpropagation employing the current dataset to perform focused learning, identify the maximized reward, and improve RA's accuracy and efficiency [52]. $P(\pi)$ represents the probability distribution function associated with (x) domains $\pi = \{\pi^1, \pi^2, \ldots, \pi^n\}$ when training the DL agents and learning is transferred to the (y) domain.

$$D^x = \{\pi^x, P(\pi^x)\}, T^x = \{y^x, f^x(\cdot)\} \tag{27}$$

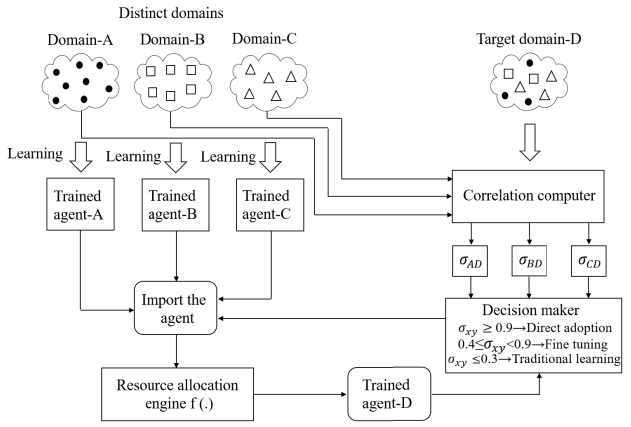

FIGURE 3. Correlation-based TL decision-making architecture.

Here, Eq. 27 represents the (x) domain D^x from where the training experiences are obtained through the TL model T^x. The imported pre-trained model T^x from the (x) domain D^x is applied to the (y) domain D^y to perform the RA as defined in Eq. 28. $f^y(\cdot)$ is a function that employs additional NN layers to perform FT on the received model of the T^x as shown below,

$$D^y = \{\pi^y, P(\pi^y)\}, T^y = \{y^y, f^y(\cdot)\} \tag{28}$$

Though TL curtails CT significantly, commemorating the high similarity between the source (x) and target (y) domains is critical. When the MU density, ν, β, Γ amidst the (x) and (y) domains are comparable, and the weighted correlation factor is exorbitant, employing the TL, the (x) domain's training experience is imported to the (y) domain via TL.

$$D^x \neq D^y, \ T^x \neq T^y \tag{29}$$

Moreover, the Eq. 29 restricts the source domain D^x and target domain D^y to be distinct when transferring the learned model T^x and applying it as T^y in the target domain for RA as shown above.

$$\sigma_{x,y} = \frac{a \cdot \mathcal{I}_x + b \cdot \nu_x + c \cdot \beta_x^{avg} + d \cdot \gamma_x^{avg}}{a \cdot \mathcal{I}_y + b \cdot \nu_y + c \cdot \beta_y^{avg} + d \cdot \gamma_{m,y}^{avg}} \tag{30}$$

$$\sigma_{x,y} \begin{cases} \geq 0.9 \text{ (direction adoption)} \\ [0.4, 0.9) \text{ (FT)} \\ \leq 0.3 \text{ (TrdL)} \end{cases} \tag{31}$$

Furthermore, Eq. 30 and 31 presents the weighted correlation factor σ_{xy} and adoption criteria as shown above. If the weighted correlation factor is inferior and the parameters between (x) and (y) domains are not comparable, TL fails to predict the accurate outcome. Therefore, TL is ideal when the correlation factor is high. When the correlation factor is low, Traditional Learning (TrdL) commences the learning process from scratch. On the contrary, the (x) and (y) domains are profoundly similar, i.e., $\sigma_{xy} \geq 0.9$, and the training experience is directly adopted. When $\sigma_{xy} \in [0.4, 0.9)$, the proposed methodology adopts the transferred model from the source domain and performs the FT [53]. If $\sigma_{xy} \leq 0.3$, as the correlation factor is deficient, TrdL is performed. Here, $\sigma_{x,y}$ indicates the correlation factor between source (x) and target (y) domains. $\mathcal{I}_x$, ν_x, β_x^{avg}, γ_x^{avg}-m, denote MU density, NSA, average nodes' *RBIs* and Γ in the (x) domain respectively while $\mathcal{I}_y$, ν_y, β_y^{avg} and γ_y^{avg}-m denote the same in the (y) domain. a, b, c, d indicate the weight factors [53].

IV. PROPOSED DL-BASED ENERGY, SPECTRUM, AND SINR-MARGINS TRADE-OFF ENABLED STRATEGIES FOR RESOURCE ALLOCATION

The precedent inquisitions evidence a trade-off between EE and SE in wireless communication; to proliferate EE, SE is sacrificed, and vice versa [14], [15], [16], [17], [18]. On the one hand, the communication devices are prophesied to function in an energy-efficient mode and transmit curtailed power; on the other hand, in 6G, THz frequencies incur excessive PLs [13]. Consequently, high-power beamforming is essential, accomplishing improved Γ and exorbitant reach at the expense of a lower EE. Furthermore, retrieved SE inflicts confined spectrum allocation, which is affected by impairments, further diminishing the Γ. Moreover, optimal relay selection considering the RBI values and spectrum defragmentation is essential in the RA, simultaneously enhancing the EE, SE, and Γ. Therefore, to perpetuate the trade-off between SE, EE, and Γ in the following subsections, the proposed DL-based methodological strategies are detailed.

A. DL-BASED GS-GT-BASED OPTIMAL PATHFINDER (GS-GTOPF)

Fig. 4(a) illustrates a transmission scenario from MU A to C, encompassing a primary path A-B-C and secondary paths A-D-C and A-E-C. This depiction considers various parameters such as RBI levels, transmitted powers, Γ, and NSA. Operating at THz frequencies incurs substantial PL, necessitating higher transmitted power. However, the limited battery life of MUs constrains the feasibility of increased power transmission due to increased energy consumption, thereby reducing EE. Furthermore, the congestion levels in the accessible spectrum differ between paths ABC and ADC, with ABC exhibiting lower congestion and higher SE, making it the preferred choice for primary transmission. To mitigate impairments, a desired Γ level, typically 1-2 dB is sought, compelling MU-A to transmit at higher power levels, thereby compromising EE. This highlights the inherent trade-off between Γ and EE in the transmission process. Moreover, spectrum sensing techniques are employed to identify suitable spectrum, thereby reducing interference and improving Γ, particularly evident in paths ABC and AEC.

However, to prevent spectrum fragmentation, we circumscribe a congested spectrum but a few disengaged slots (e.g., path ADC), which can be assigned for the imminent service request if the Γ is adequate. In such instances, we migrate services to path ADC and configure the superfluous resources into sleep mode. Fig. 4(b) exhibits the GS matrix [50]

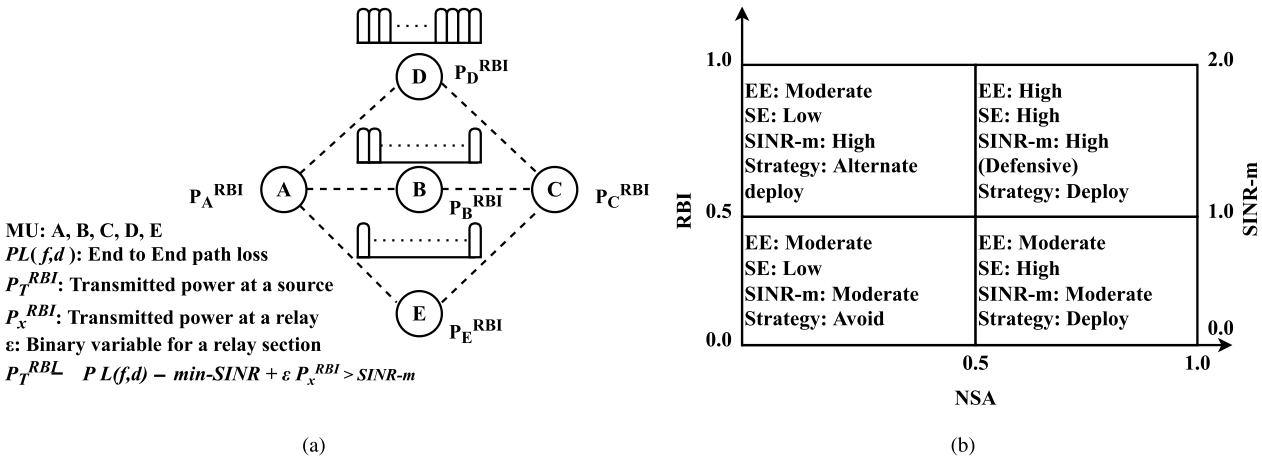

FIGURE 4. (a) RA for various spectrum scenarios (b) GS matrix depicting RA strategies.

TABLE 3. GS-GT oriented intelligent relay selection, maintaining the optimal trade-off between EE, SE, and SINR-margin (≥1: defensive, ϵ[0,1]: aggressive, ≤0.5: very aggressive).

RBI	NSA	Γ	EE	SE	Deployment decision
> 0.5	> 0.5	> 1	High	High	Highly preferred
> 0.5	< 0.5	> 1	High	Medium	Preferred
$[0.3, 0.5]$	> 0.5	$[0, 1]$	Moderate	High	Moderately preferred
$[0.3, 0.5]$	< 0.5	$[0, 1]$	Moderate	Low	Least preferred
< 0.3	> 0.5	< 0.5	Low	High	EH mode
< 0.3	< 0.5	< 0.5	Low	Moderate	

employed by the GT to determine the optimal relay while adjusting the adequate trade-off between EE, SE, and Γ. Applying the GT and GS jointly, as rendered in Fig. 4(b) and Table 3, considering the RBIs, NSAs, and Γ, an optimal path is chosen. A path comprised of relays with $\beta_n \geq 0.5$ and $\nu \geq 0.5$ demonstrates higher EE, SE, and defensive $\Gamma \geq 1$. The higher RBI enables MU to transmit higher power and extends the transmission reach. Also, a higher NSA indicates that fewer MUs operate that spectrum, resulting in reduced interference and enriched SE and Γ.

In addition, the effective distribution of the traffic over an unused spectrum improves spectrum utilization. Thus, the DL agent conjectures to deploy such a relay in the path with higher preference. $\beta_n \geq 0.5$ and $\nu < 0.5$ represent that NSA is low and the spectrum is occupied, allocating additional channels which increase the interference. Whereas when $\beta_n \in [0.3, 0.5]$ and $\nu \geq 0.5$, we obtain the enriched SE and moderate EE with an aggressive $\Gamma \in [0, 1]$, as the transmitted power is limited as a consequence of limited RBI. Furthermore, $\nu < 0.5$ indicates the spectrum is congested, and allocating additional channels increases inter-channel interference and diminishes the Γ. For $\beta_n \in [0.3, 0.5]$ and $\nu < 0.5$, as a consequence of lower RBI, Γ is aggressive; moreover, the spectrum is also crowded; consequently, such relays are deployed only when the other alternatives are unavailable. Similarly, when $\beta_n < 0.3$, these relays are eliminated from the selection game and configured in EH mode. For instance, the GS matrix enables multiple relays for a position; the DL agent bargains in the relay selection, enduring the tradeoff between EE, SE, and Γ.

The detailed pseudocode of the DL-based GS matrix-based GT approach is summarised subsequently in the pseudocode table (Algorithm-1) with the following notations. $\zeta_i = 0, 1,$ and 2 indicate the service status of i^{th} nodes, such as idle, transmitting (Tx), and receiving (Rx), respectively. BW_i and BW_T indicates the BW allocated to the i^{th} transmitting node and the total BW respectively. M and ϵ_o indicate the number of training samples and training epochs, respectively. $\mathcal{A}$, $\mathcal{I}$, $(\mathcal{E}_{Tx}, \mathcal{E}_{Rx})$, $\mathcal{U}$, and $\mathcal{K}$ represent the sets containing active nodes, active nodes available for fresh communication, busy (Tx, Rx) nodes, all nodes and all the possible paths from s to d, respectively. z represents the total number of paths in $\mathcal{K}$, t and q are counters.

Moreover, to generate the dataset, we conducted an exhaustive search between a (s, d) pair however restricted the maximum path length to 4. This decision was based on the observation that paths longer than 4 exhibited reduced throughput. Even when we relaxed the path length limit to 8, the dataset rarely included an optimal path longer than 4. Therefore, we limited the path length to 4, as conducting an exhaustive search for longer path lengths was deemed futile and redundant [44].

Algorithm 1 DL-Based GS-GTOPF

Initialize: $\mathcal{Z} = \{\zeta_1, \zeta_2, \ldots, \zeta_n\}$. $\mathcal{R} = \{\beta_n, n = \{1, 2, \ldots N\}$. $\mathcal{BW} = \{BW_1, BW_2, \ldots, BW_n\} \mid BW_i \neq 0 if\, \zeta_i = 1$. $\mathcal{A} = \mathcal{I} = \mathcal{E}_{Tx} = \mathcal{E}_{Rx} = \varnothing$. $\mathcal{U} = \{1, 2, \ldots, N\}$. $t = q = 0$.
Inputs: $(s, d) \mid (s, d) \in \mathcal{U}$
Repeat until: $t = M$
  $\mathcal{X} \leftarrow \mathcal{U} - ((s, d))$ ▷ Node numbers except (s, d).
  $\mathcal{A} \leftarrow (\mathcal{A} \cup \mathcal{X}_n) \mid \beta_n \geq 0.3, \mathcal{X}_n \in \mathcal{X}$ ▷ Active nodes.
  $\mathcal{E}_{Tx} \leftarrow (\mathcal{E}_{Tx} \cup \mathcal{X}_n) \mid \zeta_n = 1, \mathcal{X}_n \in \mathcal{X}$ ▷ Transmitting nodes.
  $\mathcal{E}_{Rx} \leftarrow (\mathcal{E}_{Rx} \cup \mathcal{X}_n) \mid \zeta_n = 2, \mathcal{X}_n \in \mathcal{X}$ ▷ Receiving nodes.
  $\nu = \frac{BW_T - \sum_{n=1}^{N} BW_n}{BW_T}$ and compute channel matrix $|\mathbf{H}|$.
  $\mathcal{I} \leftarrow \mathcal{A} - (\mathcal{E}_{Tx} \cup \mathcal{E}_{Rx})$ ▷ The active nodes available for new transmissions.
  $\mathcal{P}_N \leftarrow \{p_1, \ldots, p_n\} \mid p_i \neq 0, \forall i \in \mathcal{I}$ ▷ p_i is the allocated power using Eq. 3
  $\mathcal{K} \leftarrow \mathbb{P}(\mathcal{I} \cup (s, d)) \mid 2 \leq \textbf{length}(\mathcal{K}_i) \leq 4, 1 \leq i \leq z$ ▷ Generating all paths for (s, d) limiting path length to 4.
  $\mathcal{K} \leftarrow \{\mathcal{K}_1, \ldots, \mathcal{K}_z\} \mid \mathcal{K}_i \subset \{\mathcal{I} \cup (\mathcal{S}, \mathcal{D}), 1 \leq i \leq z$
  Compute $\mathcal{SE}$and$\mathcal{EE}$ ▷ Use Eq. 11. and Eq. 12.
  $y = \mathcal{K}_i \mid SE_i = \max(\mathcal{SE}), EE_i \geq 0.7 \times \max(\mathcal{EE}), \mathcal{K}_i \in \mathcal{K}$ ▷ y stores the optimal path.
  $F_{ip} = \{\mathcal{RBI}, |\mathbf{H}|, NSA, (s, d)\}$ ▷ Creating an input data point.
  Sample point = (F_{ip}, y).
  Update: $\beta_x^{avg} \leftarrow \text{avg}(\mathcal{R})$, $\textbf{length}(\mathcal{I}_x) \leftarrow \textbf{length}(\mathcal{I}) + 2$, $\nu_x^{avg} \leftarrow \nu$, $t = t + 1$.
Training: **Repeat until**: $q = \epsilon_o$ ▷ Train the model represented by Fig. 2.
  Train model with samples $(a_m, y_m)_{m=1}^{M}$.
Deployment: **While** model is active **do** in parallel
  For every input $(\widehat{s}, \widehat{d})$ produce output $\widehat{y}$.
  Compute β_y^{avg}, $\textbf{length}(\mathcal{I}_y)$, ν_y^{avg} and $\sigma_{x,y}$ [Eq. 30].
  if $\sigma_{x,y} \in [0.4, 0.9)$ **then** Perform TL by Re-training the last three layers of the model with the new data points.
Update: $\beta_x^{avg} = \beta_y^{avg}$, $\textbf{length}(\mathcal{I}_x) = \textbf{length}(\mathcal{I}_y)$ $\nu_x = \nu_y$.

B. SERVICE PRIORITY BASED GS-GTOPF (GS-GTOPF-SP)

The present algorithm introduces the service priorities, such as high (Q1), medium (Q2), and low (Q3), in the objective of GS-GTOPF. Eq. 32a(a-f) presents the conditions for selecting the optimal path, with $\rho_x^g \mid x \in [a, b]$ set when one of the conditions for service deployment g is met. Here, $\lambda_{s,d}^g$ indicates service requests between any (s, d) pair with priority g, where, $g = 1, 2$, and 3 indicate Q1, Q2, and Q3 services respectively. Q1 services are characterized as large BW and low latency, necessitating high QoSEs. Therefore, Q1 services are configured over the paths with nodes demonstrating $\mathcal{K}_i^\beta \geq 0.7$ and $\nu \geq 0.7$, maximizing the transmit power, reducing retransmissions and delay, and accomplishing defensive $\gamma_{avg}^i \geq 1.5$ as shown in [Eq. 32*a*] below. Here $\mathcal{K}_i^\beta$ and γ_{avg}^i denote the average RBI levels and the average SINR-margins of all the nodes in the path i in set $\mathcal{K}$.

$$\lambda_{s,d}^g = \lambda_{s,d}^1 \quad \text{then} \quad \rho_x^1 = \rho_a^1 \mid \mathcal{K}_i^\beta \in [0.7, 1], \nu \geq 0.7, \gamma_{avg}^i \geq 1.5, \quad \text{EE}_i \approx \text{SE}_i \approx \text{High} \tag{32a}$$

Alternatively, Q1 services are also configured over the paths with $\mathcal{K}_i^\beta \geq 0.7$ and $0.5 \leq \nu < 0.7$, incurring a minor interference accomplishing the reduced delay and $\gamma_{avg}^k \in [1, 1.5)$ as illustrated beneath in [Eq. 32*b*],

$$\lambda_{s,d}^g = \lambda_{s,d}^1 \quad \text{then} \quad \rho_x^1 = \rho_b^1 \mid \mathcal{K}_i^\beta \in [0.7, 1], \nu \in [0.5, 0.7), \gamma_{avg}^i \in [1, 1.5), \quad \text{EE}_i \approx \text{High}, \text{SE}_i \approx \text{medium} \tag{32b}$$

On the other hand, Q2 services solicit lesser BW and are delay insensitive; thus, Q2 services are configured on paths with $\mathcal{K}_i^\beta \in [0.5, 0.7)$ and $\nu \in [0.5, 0.7)$ therefore, the transmit powers are lower, resulting in increased retransmissions and larger delay avowing aggressive $\gamma_{avg}^k \in [0.5, 1)$ as shown in [Eq. 32*c*],

$$\lambda_{s,d}^g = \lambda_{s,d}^2 \quad \text{then} \quad \rho_x^2 = \rho_a^2 \mid \mathcal{K}_i^\beta \in [0.5, 0.7), \nu \in [0.5, 0.7), \gamma_{avg}^i \in [0.5, 1), \quad \text{EE}_i \approx \text{Medium}, \text{SE}_i \approx \text{High} \tag{32c}$$

Furthermore, if the $\nu \in [0.5, 0.7)$ is unavailable, Q2 services are also configured with $\nu < 0.5$ with very aggressive $\gamma_{avg}^k < 0.5$ as given in [Eq. 32*d*],

$$\lambda_{s,d}^g = \lambda_{s,d}^2 \quad \text{then} \quad \rho_x^2 = \rho_b^2 \mid \mathcal{K}_i^\beta \in [0.5, 0.7), \nu < 0.5, \gamma_{avg}^i < 0.5, \quad \text{EE}_i \approx \text{Medium}, \text{SE}_i \approx \text{Low} \tag{32d}$$

Finally, Q3 services requisition the least BW and are delay insensitive. Thus, they are configured over the paths with nodes demonstrating $\mathcal{K}_i^\beta \in [0.3, 0.5)$ and $\nu \geq 0.5$ and/or $\nu < 0.5$, transmitting lesser powers.

$$\lambda_{s,d}^g = \lambda_{s,d}^3 \quad \text{then} \quad \rho_x^3 = \rho_a^3 \mid \mathcal{K}_i^\beta \in [0.3, 0.5), \nu \geq 0.5, \gamma_{avg}^i < 0.5, \quad \text{EE}_i \approx \text{Low}, \text{SE}_i \approx \text{High} \tag{32e}$$

This results in more retransmissions, incurring increased delay. This aggressive behavior is demonstrated by $\gamma_{avg}^k < 0.5$, as shown below in subsequent equations [Eq. 32*e*] and [Eq. 32*f*] respectively,

$$\lambda_{s,d}^g = \lambda_{s,d}^3 \quad \text{then} \quad \rho_x^3 = \rho_b^3 \mid \mathcal{K}_i^\beta \in [0.3, 0.5), \nu < 0.5, \gamma_{avg}^i < 0.5, \quad \text{EE}_i \approx \text{Low}, \text{SE}_i \approx \text{Medium} \tag{32f}$$

If adequate resources are unavailable, services are scheduled in a waiting queue; however, a threshold timeout, τ_{th}, is configured.

C. GS-GTOPF-SP WITH REDUCED CT (GS-GTOPF-SP-RCT)

For a given (s, d) pair, an exhaustive search for an optimal path solving Eq. 12 is not feasible as the total number of paths grows exponentially with N. Furthermore, Eq. 12 is neither isotonic nor monotonic and cannot be solved using Dijkstra, and Bellman-Ford algorithms [48]. However, the authors in [49] presented a novel method, deriving the optimal solutions in polynomial time, employing an iterative usage of the shortest path with complexity $\mathcal{O}(N^4)$. The hop-count $|\mathcal{K}_i|$ for any path i^{th} path $\mathcal{K}_i$ (in an N-node network) can only take the values 1, 2, . . ., $N-1$. Therefore, Eq. 12 is solved by searching over all possible values of $|\mathcal{K}_i|$. It is an implicit property of the Bellman-Ford algorithm [45] that, at its h^{th} iteration, it identifies the optimal path between (s, d) among paths of at most h hops. Assuming, $w_{i,j}$ represents the width of the link between the i^{th} and j^{th} node as $w_{i,j} = \log_2(1+\text{SINR}_n^k)$ and $\overline{w}_i^h$ be the width of the widest path from the source node s to any other node i such that the path has at most h hops.

$$if \min(\overline{w}_i^{h-1}, w_{i,j}) > \overline{w}_i^h \quad then \quad \overline{w}_i^h = \min(\overline{w}_i^{h-1}, w_{i,j}) \tag{33}$$

The above-mentioned Eq. 33 denotes the modified Bellman-Ford condition used to find the widest path. $|\widehat{\mathcal{K}}_j^h|$ is the hop-count of the widest path from s to node j such that the path has at most h hops. $pred_j^h$, which is the predecessor of node j on the widest path from source node, s such that the path has at most h hops. The present algorithm incorporates the GS-GT-based bargaining conditions in selecting the nodes and integrates the method described in [45] to identify the best path. The hybrid GS-GT-based approach reduces the number of nodes considered during the best path discovery, substantially reducing complexity to $\mathcal{O}(N^3)$. The detail of the present algorithm is explained through the pseudocode in Algorithm 3.

D. GS-GTOPF-SP-RCT WITH ANGLE CRITERIA (GS-GTOPF-SP-RCT-θ)

GS-GTOPF-SP-rCT incorporated the GS-GT-based approach for finding the shortest path between any (s, d) pair in an optimal polynomial time. However, with the increased MU density, the CT of the GS-GTOPF-SP-rCT is increased, and efficiency decreases. GS-GTOPF-SP-rCT-θ implements a novel method leveraging the increased MU density by employing the angle-based shortest pathfinding method to reduce the CT and improve efficiency. GS-GTOPF-SP-rCT-θ forms a cone with an apex threshold angle, θ_{th} and considers the reduced number of nodes when finding the optimal paths; furthermore, nodes not complying with the GS-GT conditions are eliminated. As MU density increases, more nodes eligible for transmission will lie within the cone between the S and D, thereby increasing the probability of finding an optimal path at a reduced CT. Furthermore, the shortest path with high-power pencil beamforming at a small angle increases Γ. Fig. 5(a) demonstrate the cell with lower node density while Fig. 5(b) and Fig. 5(c) show the cell with higher node density. It is observed from Fig. 5(c) that increased MU density of $N = 30$ and reduced $\theta_{th} = 60$ significantly reduces the number while maintaining an optimal trade-off between SE, EE, and Γ, maintaining CT lower when finding the best path.

Algorithm 2 GS-GTOPF-SP

1: **Initialize:** Same as DL-based GS matrix-based GT algorithm. τ(timeout counter) $= 0$
2: **Inputs:** $\lambda_{s,d}^g$, $(s, d) \mid s,d \in \mathcal{U}$
3: $\mathcal{K}^\beta \leftarrow \{\mathcal{K}_1^\beta, \mathcal{K}_2^\beta, \ldots, \mathcal{K}_z^\beta\} \mid \mathcal{K}_i^\beta = \frac{\sum_{\forall j \in \mathcal{K}_i} \beta_j}{\textbf{length}(\mathcal{K}_i)}$, $\mathcal{K}_i \in \mathcal{K}$, $1 \le i \le z$
4: **if** $\lambda_{s,d}^g == \lambda_{s,d}^1$ **then**
5: **if** $\exists\ \mathcal{K}_i \mid \mathcal{K}_i^\beta \ge 0.7$, $\nu \ge 0.7$ and $\gamma_{avg}^i \ge 1.5$ **then**
6: $\mathcal{SE} \leftarrow \{SE_1, SE_2, \ldots, SE_z\}$ where $\forall\ SE_i \mid \mathcal{K}_i^\beta \ge 0.7$
7: Deploy on path $K_i \mid SE_i = \max(\mathcal{SE})$, $\mathcal{K}_i^\beta \ge 0.7$, $\nu \ge 0.7$ and $\gamma_{avg}^i \ge 1.5$
8: **else if** $\exists\ \mathcal{K}_i \mid \mathcal{K}_i^\beta \ge 0.7$, $\nu \in [0.5, 0.7)$ and $\gamma_i \in [1, 1.5)$ **then**
9: $\mathcal{SE} \leftarrow \{SE_1, SE_2, \ldots, SE_z\}$ where $\forall\ SE_i \mid \mathcal{K}_i^\beta \ge 0.7$
10: Deploy on path $K_i \mid SE_i = \max(\mathcal{SE})$, $\mathcal{K}_i \ge 0.7$, $\nu \in [0.5, 0.7)$ and $\gamma_i \in [1, 1.5)$
11: **else if** $\tau > \tau_{th}$ **then** Drop service request and timeout of the algorithm
12: $\tau = \tau + 1$; Wait and go back to step 3
13: **else if** $\lambda_{s,d}^g == \lambda_{s,d}^2$ **then**
14: **if** $\exists\ \mathcal{K}_i \mid \mathcal{K}_i^\beta \in [0.5, 0.7)$, $\nu \in [0.5, 0.7)$ and $\gamma_i \in [0.5, 1)$ **then**
15: $\mathcal{SE} \leftarrow \{SE_1, SE_2, \ldots, SE_z\}$ where $\forall\ SE_i \mid \mathcal{K}_i^\beta \in [0.5, 0.7)$
16: Deploy on path $\mathcal{K}_i \mid \mathcal{K}_i^\beta \in [0.5, 0.7)$, $\nu \in [0.5, 0.7)$ and $\gamma_i \in [0.5, 1)$
17: **else if** $\exists\ \mathcal{K}_i \mid \mathcal{K}_i^\beta \in [0.5, 0.7)$, $\nu < 0.5$ and $\gamma^k < 0.5$ **then**
18: $\mathcal{SE} \leftarrow \{SE_1, SE_2, \ldots, SE_z\}$ where $\forall\ SE_i \mid \mathcal{K}_i^\beta \in [0.5, 0.7)$
19: Deploy on path $\mathcal{K}_i \mid \mathcal{K}_i^\beta \in [0.5, 0.7)$, $\nu \le 0.5$ and $\gamma_i < 0.5$
20: **else if** $\tau > \tau_{th}$ **then** Drop service request and timeout of the algorithm
21: $\tau = \tau + 1$; Wait and go back to step 3
22: **else** $\lambda_{s,d}^g == \lambda_{s,d}^3$ **then** repeat the process from point no.13 for specified conditions.
23: $\tau = \tau + 1$; Wait and go back to step 3

V. SIMULATIONS AND RESULTS

A. SIMULATION ENVIRONMENT

The present section exhibits the comprehensive simulation results of the proposed strategies. The simulation studies employed Matlab 2021a and the Jupiter notebook with a Python interface with TensorFlow libraries, a system with Intel i7 octa-core CPU, 4Gb NVIDIA Quadro Q1000 GPU, and 64 Gb RAM. The simulation parameters employed

Algorithm 3 GS-GTOPF-SP-rCT

1: **Initialize:** Same initialisation as GS-GTOPF algorithm. Let $\overline{w}_s^h = \infty$, for $h = 0, 1, \ldots, N-1$ and $\overline{w}_i^0 = 0$, $\forall\, i \neq s$. Let $|\widehat{\mathcal{K}_s^h}| = 0$ for $h = 0, 1, \ldots, N-1$ and $|\widehat{\mathcal{K}_i^0}| = \infty\ \forall\, i \neq s$.
2: **Inputs:** $(\mathcal{S}, \mathcal{D}) \mid \mathcal{S}, \mathcal{D} \in \mathcal{U}$
3: Follow steps 4-10 as indicated in the GS-GTOPF algorithm.
4: **for** $h = 1, 2, \ldots, N-1$ **do**
5: $\quad \forall\, i \in N\, do \overline{w}_i^h = \overline{w}_i^{h-1}$
6: $\quad \forall\, (i, j) \in N$ **do**
7: $\quad$ **if** $\min(\overline{w}_i^{h-1}, w_{i,j}) > \overline{w}_i^h then \overline{w}_i^h = \min(\overline{w}_i^{h-1}, w_{i,j})$; $|\widehat{\mathcal{K}}_j^h| = |\widehat{\mathcal{K}}_j^{h-1}| + 1$; $pred_j^h = i$
8: Compute $\widehat{\mathcal{J}}^h = \frac{W_d^h}{|\widehat{\mathcal{K}_d^h}|}$ ▷ For a path with h hops, $\widehat{\mathcal{J}}^h$ is the optimal SE.
9: Return the path with largest $\widehat{\mathcal{J}}^h$.

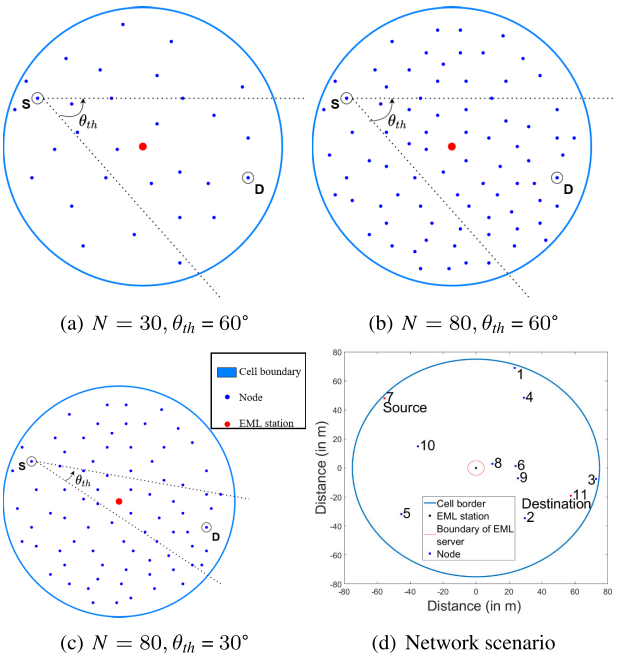

(a) $N = 30, \theta_{th} = 60°$ (b) $N = 80, \theta_{th} = 60°$
(c) $N = 80, \theta_{th} = 30°$ (d) Network scenario

FIGURE 5. Node density to illustrate the effectiveness of GS-GTOPF-SP-rCT-θ.

during the investigation are epitomized in Table 4. Fig. 5(d) illustrates a pilot network scenario with randomly generated MU nodes within a radius of 75m. As per the PT and EH models explained in Section II, only the nodes with $\beta_n \geq 0.3$ can participate in establishing the communication. Whereas nodes ($\beta_n \leq 0.3$) are configured in the EH mode and join after the EH cycle or during the scarcity. For the presented case in Fig. 5(d), ($S = 7$, $D = 11$) is designated a target (s, d) pair for initiating the transmission. For simplicity, we explain one path; however, the dynamic situation is simulated considering the multipath transmissions simultaneously. Furthermore, to study the behavior of SE, EE, and Γ, we configure the Single Input Single Output

Algorithm 4 GS-GTOPF-SP-rCT-θ

1: **Initialize:** Same initialisation as GS-GTOPF-SP-rCT algorithm.
2: **Inputs:** $(s, d) \mid s, d \in \mathcal{U}$
3: Follow steps 4-10 as indicated in the GS-GTOPF algorithm.
4: Let $\mathcal{D} = \{\vec{d}_{s,1}, \vec{d}_{s,2}, \ldots, \vec{d}_{s,z}\}$ ▷ $\mathcal{D}$ is a set of vectors from source to every other node in $\mathcal{I}$.
5: $\mathcal{T} = \varnothing$ ▷ $\mathcal{T}$ is a set of all the angles between the vector $\vec{d}_{s,d}$ and $\vec{d}_{s,i}$, $\forall\ 1 \leq i \leq z$.
6: $\mathcal{T} \leftarrow \mathcal{T} \cup \theta_i \mid \theta_i = \frac{\vec{d}_{s,d} \cdot \vec{d}_{s,i}}{|\vec{d}_{s,d}||\vec{d}_{s,i}|} \leq \theta_{th}\ \forall\ 1 \leq i \leq z$.
7: $\mathcal{I}' = \varnothing$ ▷ $\mathcal{I}'$ contains the set of the reduced number of nodes considering the angle condition.
8: $\mathcal{I}' \leftarrow \mathcal{I}' \cup \mathcal{I}_i \mid |\theta_i| \geq \theta_{th}$ or $|\vec{d}_{s,i}| \leq d_{th}$.
9: Follow steps 4-9 as indicated in GS-GTOPF-SP-rCT.

TABLE 4. Key parameters for network simulation [13], [54], [55], [56].

Sl. No.	Parameter	Specifications
1	β_n value (Random variable)	$\mathcal{N}(0.5,\ 0.1)$
2	Minimum received SINR threshold	-115 dBm
3	Probability of service (Q1, Q2, and Q3)	0.5, 0.3 and 0.2
4	Single channel BW	1 GHz
5	Frequency range	0.1 - 1 THz
6	χ_{shd} shadow fading standard deviation	3.14 dB
7	Interference power	3 dBm
8	AWGN power variance	-174 dBm/Hz

(SISO), 4×4, 16×16, and 32×32 MIMO. As demonstrated in Fig. 2, a multi-input DNN architecture is employed to ascertain the resource-efficient path between each (s, d) pair in the network. DNN model receives the channel matrix, RBIs of the participating nodes, NSAs of the participating links, and (s, d) pairs branching in four separate streams. The outputs of these branches are concatenated and further processed to identify the resource-efficient path. The base model is constructed for $N = 30$ nodes in the cell. The model trains over 150,000 samples for 2,500 epochs within 52,800 seconds, considering batches of 64 and is then tested for over 30,000 samples.

B. RESULTS AND DISCUSSION

Fig. 6 presents the average SE and EE performance for the increased number of intermediate nodes in the transmission path for a given (s, d) pair. The SE and EE values are averaged across all the available paths for any (s, d) pair, e.g., SE and EE are computed by averaging across all the paths with one intermediate node. Fig. 6 depicts that average SE emerges preeminent when considering the paths comprised of one intermediate node leveraging the spectrum fragmentation, whereas average EE is superlative for paths with no intermediate nodes. As a result, the path with one intermediate node is recommended for applications prioritizing SE with modest EE sacrifice. Conversely, the direct path is recommended for EE, incurring a minor drop in SE. Therefore the optimal trade-off between SE

and EE is preserved. In case when neither the two-hop path nor the direct path between a (s, d) pair is available, a path with a higher number of intermediate nodes is recommended, sacrificing SE and EE in exchange for the reduced service waiting period. However, delay-insensitive services are scheduled in a queue until an efficient path evolves. Furthermore, THz frequencies incur larger PLs, degrading the signal strength and Γ. Therefore, determining a path with an optimal number of intermediate nodes over any (s, d) pair maintains the trade-off between SE, EE, and Γ. Fig. 6 demonstrates SE and EE for SISO and MIMO with 4×4, 16×16, and 32×32 degrees, respectively. We noted a substantial improvement in SE and EE employing MIMO with an increased degree than SISO. Considering a path with one intermediate node between any (s, d) pair, the average SE is observed to be -31.91, 2.40, 5.70, and 7.34 dB, and EE comes out to -35.23, -0.91, 2.38, and 4.01 dB for SISO, 4×4, 16×16, and 32×32 MIMO, respectively.

Fig. 7(a) and 7(b) demonstrate the normalized Γ and BER according to the intermediate nodes for any (s, d) pair, respectively. As exhibited in Fig. 7(a), the direct path (SISO) demonstrates an Γ of 0.396 dB, and paths with one and two intermediate nodes exhibit enhanced Γ of 0.45 and 0.46 dB, respectively. The intermediate nodes regenerate the signal, ameliorating the Γ. However, the paths with three or more intermediate nodes reveal lower advancement in Γ. Furthermore, to improve the Γ, massive MIMO is employed. As depicted in Fig. 7(a), Γ employing 4×4, 16×16, and 32×32 MIMO for paths with one intermediate node displays 0.92, 1.34, and 1.75 dB, respectively. In the present investigation, numerous paths as per the intermediate nodes for any (s, d) pair are determined, and the average Γ values are computed. For example, for any (s, d) pair with one intermediate node employing 16×16 MIMO, if five alternate paths are determined, the Γ are averaged across them, and the path with the largest Γ above the average is commissioned. As illustrated in Fig. 7(b), considering the 32×32 MIMO configuration, BER for the paths with one and two intermediate nodes are 0.15×10^{-3} and 0.17×10^{-3} Bits Per Second (bps), respectively, which is much lesser than the direct path leading to the higher BER of 0.99×10^{-3} bps. As a result of the intermediate node acting as a regenerator, the SINR performance is improved substantially, lowering BER.

Furthermore, as shown in Fig. 6, commissioning paths with one intermediate node improves SE by leveraging spectrum fragmentation, whereas, beyond two intermediate nodes, SE decays. On the contrary, EE is the maximum for direct paths, whereas employing the paths with increased intermediate nodes engages more transmission equipment, squandering higher power costs. Therefore, obtaining the optimal tradeoff between SE, EE, and Γ is essential. From Fig. 6, 7(a), and 7(b), for 32×32 MIMO, commissioning the paths with one node demonstrates maximal SE of 7.34 dB, EE of 4.01 dB, Γ of 1.75 dB, and BER of 0.15×10^{-3} bps. Similarly, commemorating the paths with two intermediate nodes employing 32×32 MIMO demonstrates SE of 5.65 dB, EE of 0.46 dB, Γ of 1.88 dB, and BER of 0.17×10^{-3} bps. Consequently, modest sacrifice in EE results in significant improvements in SE, Γ, and BER. Direct transmission achieves maximum EE; however, SE (bps/Hz) is lower by 17.37% and Γ lower by 12.97% from their respective peaks. At one intermediate node, maximum SE is achieved; however, EE (bits/J/Hz) is lower by 17.28% and Γ lower by 3.39% from their respective peaks. When maximum Γ is reached, the SE (bps/Hz) is lower by 82.08%, and EE (bits/J/Hz) is lower by 97.20% from their respective peaks. As shown in Fig. 6, considering the paths with one intermediate node, MIMO with 4×4, 16×16, and 32×32 configurations demonstrate 34.31dB, 37.618dB, and 39.253 dB higher SE than SISO, respectively; furthermore, 34.32 dB, 37.618 dB, and 39.253 dB higher EE than SISO, respectively. Moreover, the aforementioned tradeoff is also valid when energy is the bottleneck. To accomplish amended EE, as presented in Fig. 6, 7(a), and 7(b), for 32×32 MIMO, commissioning the direct paths demonstrate maximal EE of 6.78 dB, SE of 6.82 dB, Γ of 0.80 dB, and BER of 0.99×10^{-3} bps.

Table 5 compares the CT in training, testing, and accuracy for TrdL and TL approaches (the entity with 0 is the initial reference point for the comparison). Fig. 7(c) and 7(d) demonstrate CT and accuracy according to MU density for TrdL and TL with (w) and without (w/o) FT. To investigate TL's behavior, a pre-trained model with $N = 30$ is employed. We also performed the TrdL, considering N of 10, 15, 20, and 25 nodes. The accuracy and CT to train and test the TrdL model are computed as a reference for the TL approaches. TL without FT (TLw/oFT) approach adopts the transferred model, i.e., $N = 30$, and inspects the accuracy of the base model's predictions on the target domain's new data inputs. On the other hand, as shown in Fig. 2, TL with FT (TLwFT) performs FT on the last three FC layers of the received model. Fig. 7(d) and Table 5 infer that TLwFT demonstrates superior accuracy compared with TLw/oFT and TrdL approaches. Furthermore, Fig. 7(c) and Table 5 infer that TrdL incurs increased CT compared with TL approaches, whereas TLwFT incurs increased CT compared with TLw/oFT but accomplishes the highest accuracy. However, TLw/oFT demonstrates acceptable accuracy incurring the least CT compared with TrdL and TLwFT approaches. As summarized in Table 5, on an average, TLw/oFT incurs 94.19% reduced CT and 18.25% increased accuracy compared to TrdL over all cases of N. On the other hand, TLwFT incurs 43.18% reduced CT and 3.71% increased accuracy compared to TrdL. Similarly, TLw/oFT incurs approximately 89.78% lesser time cost over TLwFT. Overall, TLwFT provides 26.90% more accuracy than TLw/oFT, averaged over all cases of N. Therefore, the TLwFT approach is used whenever there is a change in the network parameters instead of creating a new model and re-training it entirely.

Fig. 8(a), 8(b), and Table 6 demonstrate the behaviours of CT and accuracy for TrdL, TLwFT, and TLw/oFT in

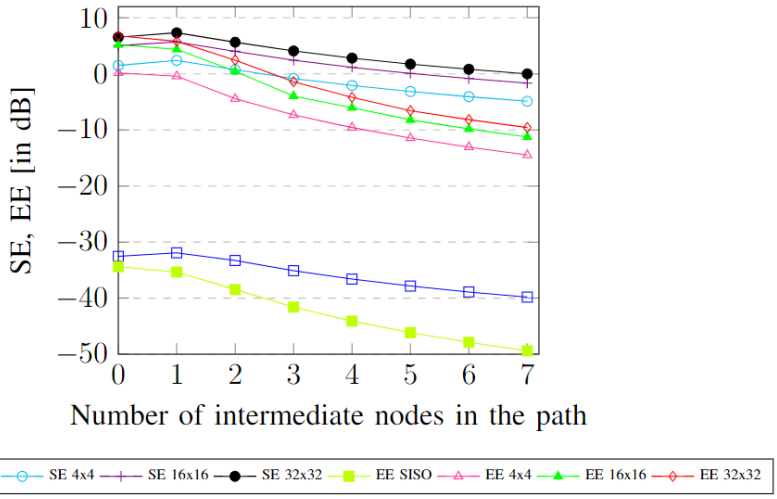

FIGURE 6. Average SE and EE Vs. number of intermediate nodes.

TABLE 5. CT vs. MU's density with training samples of 50k and testing samples of 10k.

	TrdL				TL							
					Without FT				With FT			
N	10	15	20	25	10	15	20	25	10	15	20	25
CT (*seconds*)	1.22k	1.21k	1.28k	1.27k	60.1	68.67	75.25	86.77	694.3	698.3	722.7	727.41
Relative CT (%)	0	0	0	0	−95.08	−94.36	−94.15	−93.19	−43.17	−42.69	−43.90	−42.97
Relative CT (%)	-	-	-	-	−91.34	−90.16	−89.58	−88.07	0	0	0	0
Acc. (%)	86.59	80.27	76.10	72.58	69.28	64.94	62.56	60.87	89.20	82.95	79.10	75.90
Relative acc. (%)	0	0	0	0	19.99	19.09	17.79	16.13	3.01	3.33	3.94	4.57
Relative acc. (%)	-	-	-	-	0	0	0	0	28.75	27.73	26.43	24.69

TABLE 6. CT vs. RBI mean with training samples of 50k and testing samples of 10k.

	TrdL				TL							
					Without FT				With FT			
RBI mean	0.4	0.5	0.7	0.9	0.4	0.5	0.7	0.9	0.4	0.5	0.7	0.9
CT (*seconds*)	1.40k	1.43k	1.45	1.47k	62.32	63.45	64.16	65.02	321.68	318.3	319.3	319.5
Relative CT (%)	0	0	0	0	−95.57	−95.59	−95.59	−95.58	−77.11	−77.89	−78.05	−78.28
Relative CT (%)	-	-	-	-	−80.63	−80.07	−79.91	−79.65	0	0	0	0
Acc. (%)	70.00	67.00	64.30	64.25	69.05	66.66	64.00	63.90	78.35	73.15	70.80	70.25
Relative acc. (%)	0	0	0	0	−1.36	−0.51	−0.47	−0.54	11.93	9.18	10.11	9.34
Relative acc. (%)	-	-	-	-	0	0	0	0	13.47	9.74	10.63	9.94

accordance with average RBI. A pre-trained model with $N = 30$ and $RBI_{avg} = 0.5$ is imported to predict the optimal path, maintaining the aforementioned tradeoff for varying $RBI_{avg} = 0.4$, 0.5, 0.7, and 0.9. TLw/oFT equips with an enormous reduction in CT and similar accuracy compared to TrdL, resulting in a suitable replacement of TrdL. From Table 6, it is inferred that TLw/oFT incurs, on an average, 95.56% reduced CT at a minor reduction in accuracy of 0.72% compared to TrdL. On the other hand, TLwFT furnishes the highest accuracy of all the scenarios at increased CT compared to TLw/oFT; however, TLwFT demonstrates substantially reduced CT compared to TrdL. TLwFT demonstrates, on an average 77.83% reduction in CT and a 10.14% increase in accuracy compared to TrdL. In contrast, TLw/oFT incurs, on an average 80.06% reduced CT, costing a 10.94% reduction in accuracy than TLwFT.

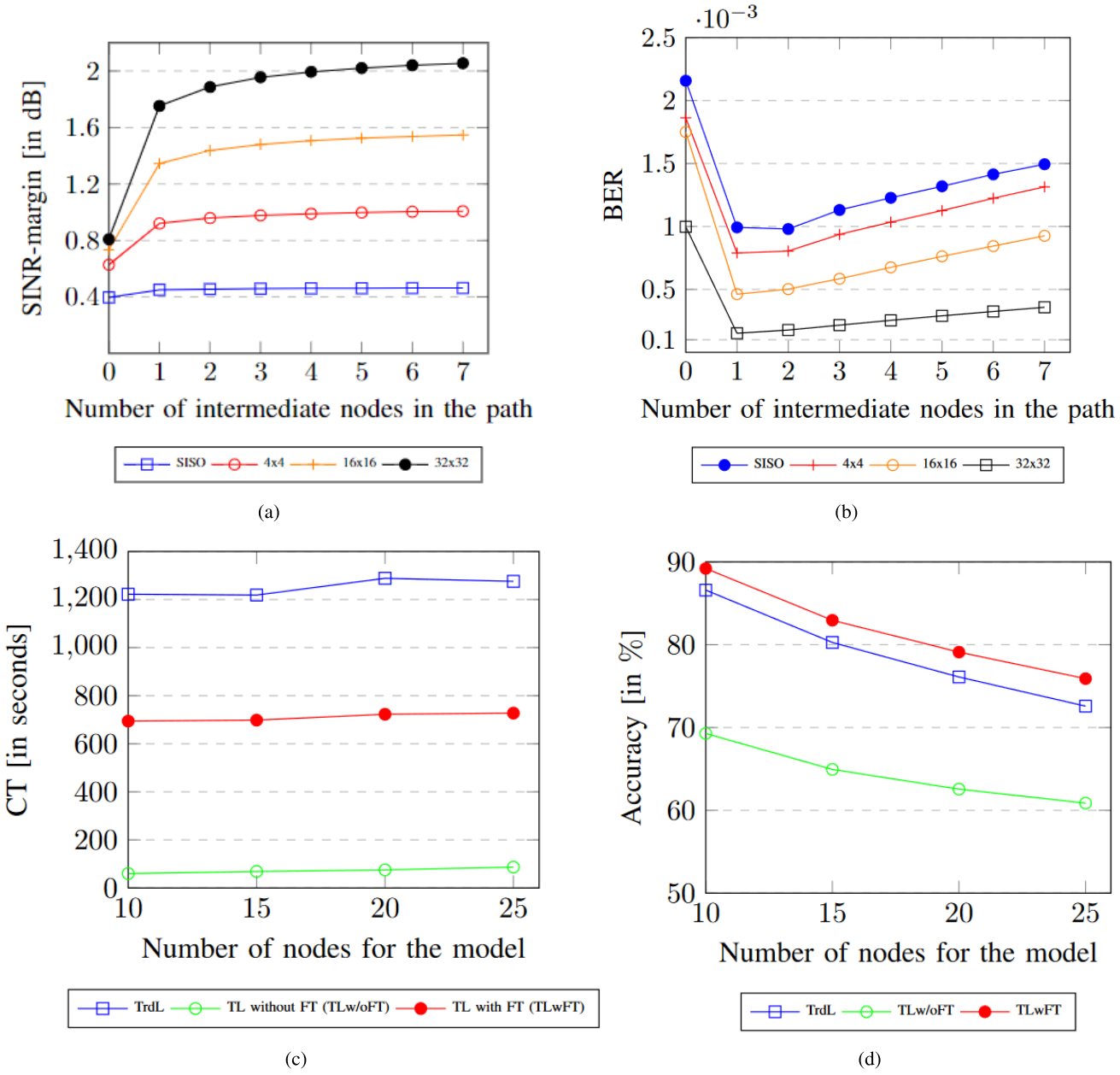

FIGURE 7. (a): SINR-margin vs. Number of intermediate nodes, (b): BER vs. Number of intermediate nodes, (c): CT with respect to MU's Density and (d): Accuracy with respect to MU's Density.

Hence, TLw/oFT is a substitute for TrdL, whereas TLwFT is suitable when accuracy is of greater importance.

Fig. 9(a) infers that with the implementation of GS-GTOPF-SP algorithm, on an average, the Q1 services incur 76.06% and 3.87% reduced latency compared to Q3 and Q2 services, respectively. As a significant portion of the resource is reserved for Q1 and Q2 services, these are expected to suffer lower delays and result in larger SE, EE, and Γ over Q3. Q1 services are deployed on the paths configured with the nodes demonstrating higher RBI values, hence transmitting the larger power (Eq. 3), achieving the optimal tradeoff between SE, EE, and Γ, resulting in improved performance. On an average, Q1 services demonstrate 12.97% and 62.55% increased SE (bps/Hz), 16.14% and 81.97% improved EE (bits/J/Hz), 12.27% and 25.95% improved Γ compared to Q2 and Q3 services, respectively. Q2 services have, on an average, 75.09% lower time delays, 43.87% greater SE (bps/Hz), 56.67% greater EE (bits/J/Hz), and 12.17% greater Γ than Q3 services.

As shown in Fig. 9(b), to determine the optimal apex angle of the cone, the relationship between the apex angle, the number of nodes (N), and the probability that the best path lies entirely inside the cone is analyzed. For the same apex angle, as the MU density increases, the probability of

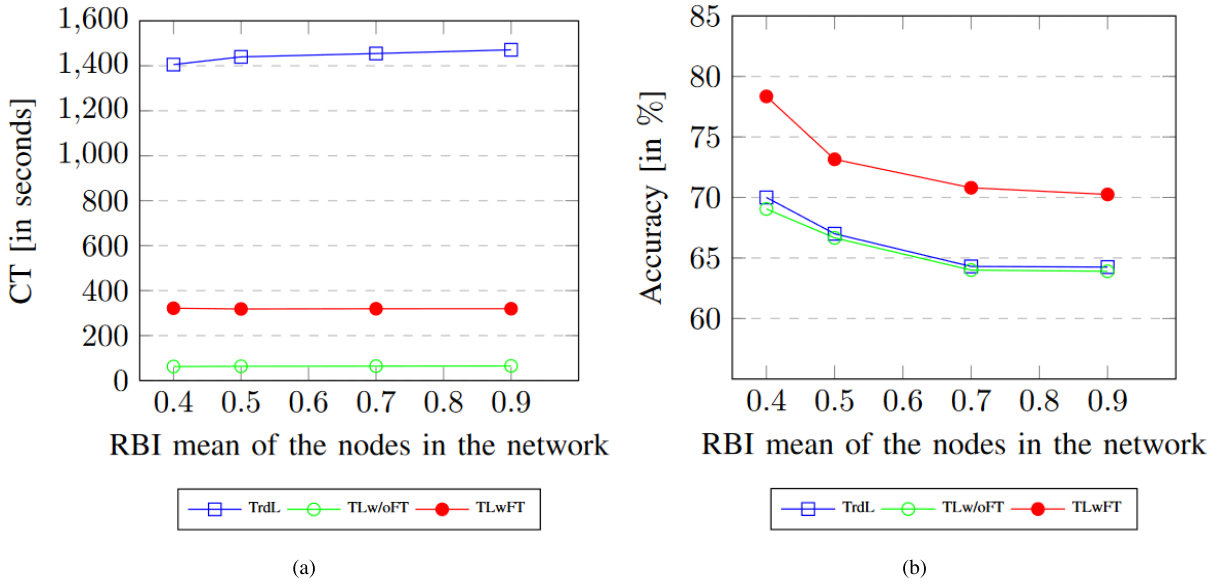

FIGURE 8. (a): CT with respect to RBI mean (b): Accuracy with respect to RBI mean.

the best path residing within the cone also increases. From Fig. 9(b), notice that the probability saturates around $\theta_{th} = 80°$, which is configured as the threshold apex angle for a cone. At $\theta_{th} = 80°$, the probability for $N = 80$ is greater by 18.07%, 11.37%, 6.55%, 3.61%, and 1.37% than at $N = 30$, $N = 40$, $N = 50$, $N = 60$, and $N = 70$, respectively. Hence, we deduce that increasing MU density is beneficial for GS-GTOPF-SP-rCT-θ. In addition, obtaining the optimal threshold angle also configures the beamforming transmitting higher power at a specified apex angle, improving the SE, EE, and Γ. To measure the adequacy of GS-GTOPF-SP-rCT-θ, Fig. 9(c) infers that for $N = 50$ at $\theta_{th} = 30°, 40°, 50°$, and $60°$, the probability that none of the nodes (zero nodes) of the best path lying outside the cone framed for finding the best path are 0.6298, 0.7584, 0.8476, and 0.9029, respectively. Therefore, as θ_{th} increases, GS-GTOPF-SP-rCT-θ accurately identifies the optimal path. Further, for $\theta_{th} = 30°$, with probabilities 0.2481, 0.0802, 0.0277, and 0.0142; 1, 2, 3, and 4 nodes of the best path lie outside the cone, respectively. For $\theta_{th} = 40°$, the probabilities correspond to are 0.1803, 0.0422, 0.0136, and 0.0055, respectively. For $\theta_{th} = 50°$, the probabilities correspond to 0.1206, 0.0231, 0.0069, and 0.0018, respectively. Further, for $\theta_{th} = 60°$, the probabilities correspond to 0.0807, 0.013, 0.0029, and 0.0005, respectively. Consequently, from Fig. 9(b) and Fig. 9(c), we can conclude that, the accuracy of GS-GTOPF-SP-rCT-θ increases by increasing θ_{th} and N. On the other hand, enlarging θ_{th} results in considering an increased number of nodes inside the cone, consequently accumulating higher CT in computing the best path for transmission, although gaining accuracy. With growing MU density, we can reduce θ_{th} and hence CT; therefore, even with an increase in N, we only consider a portion of this N present inside the cone, and there is no decrease in the accuracy of GTOPF-SP-rCT-θ. Furthermore, the reduced angle assists directional beamforming with increased transmitted power in a specific direction, improving the Γ. Hence, for $\theta_{th} \in [50, 80]$, is optimal in finding the best path.

Fig. 9(d) presents the accuracy and CT with respect to varying MU density, N, and θ_{th} for GS-GTOPF-SP-rCT-θ. Furthermore, Fig. 9(d) compares the CT for GS-GTOPF-SP-rCT and GS-GTOPF-SP-rCT-θ with respect to varying MU density N and θ_{th}. It is observed that GS-GTOPF-SP-rCT-θ consumes substantially lower CT compared to GS-GTOPF-SP-rCT. For a given N, the CT grows with the threshold angle as more nodes are eligible for consideration; however, the total time remains significantly lower than GS-GTOPF-SP-rCT. Furthermore, GS-GTOPF-SP-rCT suffers an increased rate of CT when N is significantly more. The rate of increase is $0.77ms$ per increase in 10 nodes initially, from $N = 30$ to $N = 40$ and changes to $2.01ms$ per increase in 10 nodes for N from 70 to 80, while for GS-GTOPF-SP-rCT-θ, for increase from $N = 70$ to $N = 80$, there is approximately $0.544ms$ per increase in 10 nodes for $\theta_{th} = 100$. On an average GS-GTOPF-SP-rCT-θ provides 72.77%, 75.13%, 76.52%, 77.29%, 77.57%, and 77.97% curtailment in CT over GS-GTOPF-SP-rCT for $N = 30, 40, 50, 60, 70$, and 80 respectively while maintaining an accuracy of $\geq 95\%$ for the range $\theta_{th} \in [40, 100]$. Fig. 9(d) also demonstrates that for any θ_{th} as N proliferates, the accuracy of GS-GTOPF-SP-rCT-θ is also improved. For $\theta_{th} = 60°, 80°, 90°$, and $100°$, GS-GTOPF-SP-rCT-θ demonstrates an average accuracy of 95%, 97%, 98%, and 99%. Finally, for an optimal θ_{th}, GS-GTOPF-SP-rCT-θ achieves a more significant reduction in CT, higher accuracy, and increased Γ assisted by directional beamforming.

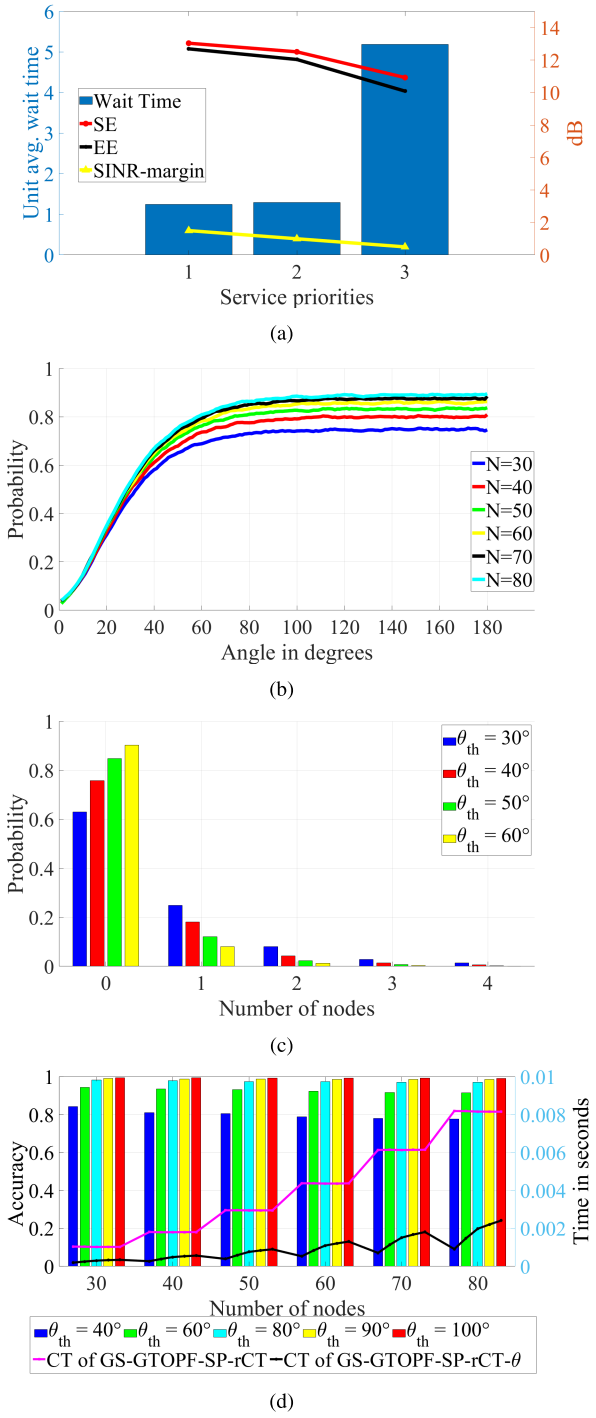

FIGURE 9. (a) Unit avg. wait time, SE, EE, and SINR-margin of services. (b) The probability that the best path lies within the angle. (c) Probability of nodes of the best path outside the cone for $N = 50$. (d) Accuracy of GS-GTOPR-SP-rCT-θ and CT of GS-GTOPF-SP-rCT and GS-GTOPR-SP-rCT-θ.

VI. CONCLUSION AND FUTURE SCOPE

The current paper proposes the DL-based RA strategical algorithms to preserve the optimal trade-off amid EE, SE, and Γ in 6G wireless networks. Our proposed work reveals that DL-oriented GS-GT-based RBI aware node and path selection adjudicate the Γ (aggressive, defensive, or moderate), ameliorates SE and EE, and curtails spectrum fragmentation substantially. In addition, incorporated TL contracts the CT and significantly elevates the prediction accuracy compared to TrdL. Firstly, the proposed GS-GTOPF algorithm demonstrates maximized EE by trading-off of 17.37% of SE (bps/Hz) and 12.97% of Γ; on the other hand, maximum SE is accomplished by trading-off EE by 17.28% and Γ by 3.39%. Secondly, the GS-GTOPF-SP demonstrates that Q1 services accomplish 3.87% and 76.06% decreased waiting period compared to Q2 and Q3 services, respectively, while attaining 12.97% and 62.55% increment in SE, 16.14% and 81.97% in EE, and further 12.27% and 25.95% in Γ, respectively. Besides, the refinement has been further advanced by reducing the CT, resulting in the GS-GTOPF-SP-rCT algorithm. Furthermore, we propose an angle criterion-based GS-GTOPF-SP-rCT-θ algorithm which leverages the increased MU density and discovers the optimal paths demonstrating a 76.12% contraction in CT over GS-GTOFP-SP-rCT accomplishing an accuracy of $\geq$ 95%. The successful outcomes of our proposed DL-based RA strategies open up several avenues for future research. One potential direction is a further exploration of the proposed algorithm's adaptability and scalability in dynamic and heterogeneous 6G networks. Integrating emerging technologies such as edge computing and quantum communication could enhance performance. Finally, extending the scope of our work to consider security and privacy implications and include real-world deployment scenarios for validation. Overall, these findings offer valuable insights for future research. Ultimately, the authors strongly believe that future research endeavours will significantly benefit from the proposals and findings presented in our work.

REFERENCES

[1] W. Jiang, B. Han, M. A. Habibi, and H. D. Schotten, "The road towards 6G: A comprehensive survey," *IEEE Open J. Commun. Soc.*, vol. 2, pp. 334–366, 2021.

[2] S. Fu, F. Yang, and Y. Xiao, "AI inspired intelligent resource management in future wireless network," *IEEE Access*, vol. 8, pp. 22425–22433, 2020.

[3] W. Saad, M. Bennis, and M. Chen, "A vision of 6G wireless systems: Applications, trends, technologies, and open research problems," *IEEE Netw.*, vol. 34, no. 3, pp. 134–142, May 2020.

[4] Q. Mao, F. Hu, and Q. Hao, "Deep learning for intelligent wireless networks: A comprehensive survey," *IEEE Commun. Surveys Tuts.*, vol. 20, no. 4, pp. 2595–2621, 4th Quart., 2018.

[5] K. B. Letaief, W. Chen, Y. Shi, J. Zhang, and Y. A. Zhang, "The roadmap to 6G: AI empowered wireless networks," *IEEE Commun. Mag.*, vol. 57, no. 8, pp. 84–90, Aug. 2019.

[6] B. Mao, Y. Kawamoto, and N. Kato, "AI-based joint optimization of QoS and security for 6G energy harvesting Internet of Things," *IEEE Internet Things J.*, vol. 7, no. 8, pp. 7032–7042, Aug. 2020.

[7] V. Pathak, R. J. Pandya, V. Bhatia, and O. A. Lopez, "Qualitative survey on artificial intelligence integrated blockchain approach for 6G and beyond," *IEEE Access*, vol. 11, pp. 105935–105981, 2023.

[8] M. Z. Chowdhury, M. Shahjalal, S. Ahmed, and Y. M. Jang, "6G wireless communication systems: Applications, requirements, technologies, challenges, and research directions," *IEEE Open J. Commun. Soc.*, vol. 1, pp. 957–975, 2020.

[9] M. Alsabah, M. A. Naser, B. M. Mahmmod, S. H. Abdulhussain, M. R. Eissa, A. Al-Baidhani, N. K. Noordin, S. M. Sait, K. A. Al-Utaibi, and F. Hashim, "6G wireless communications networks: A comprehensive survey," *IEEE Access*, vol. 9, pp. 148191–148243, 2021.

[10] E. Semaan, "6G spectrum-enabling the future mobile life beyond 2030," Ericsson, Stockholm, Swedez, White Paper no. GFTL-23:000243, Mar. 2023, https://www.ericsson.com/4953b8/assets/local/reports-papers/white-papers/6g-spectrum.pdf .

[11] NTT Docomo. (Jan. 2023). *5G Evolution and 6G, Docomo White Paper*. [Online]. Available: https://www.docomo.ne.jp/english/binary/pdf/corporate/technology/whitepaper_6g/DOCOMO_6G_White_PaperEN_20200124.pdf

[12] Huawei Technologies. (2022). *6G: The Next Horizon, Huawei White Paper*. [Online]. Available: https://www-file.huawei.com/-/media/corp2020/pdf/tech-insights/1/6g-white-paper-en.pdf?la=en

[13] T. S. Rappaport, Y. Xing, O. Kanhere, S. Ju, A. Madanayake, S. Mandal, A. Alkhateeb, and G. C. Trichopoulos, "Wireless communications and applications above 100 GHz: Opportunities and challenges for 6G and beyond," *IEEE Access*, vol. 7, pp. 78729–78757, 2019.

[14] M. Sengly, K. Lee, and J.-R. Lee, "Joint optimization of spectral efficiency and energy harvesting in D2D networks using deep neural network," *IEEE Trans. Veh. Technol.*, vol. 70, no. 8, pp. 8361–8366, Aug. 2021.

[15] O. Aydin, E. A. Jorswieck, D. Aziz, and A. Zappone, "Energy-spectral efficiency tradeoffs in 5G multi-operator networks with heterogeneous constraints," *IEEE Trans. Wireless Commun.*, vol. 16, no. 9, pp. 5869–5881, Sep. 2017.

[16] A. He, L. Wang, Y. Chen, K.-K. Wong, and M. Elkashlan, "Spectral and energy efficiency of uplink D2D underlaid massive MIMO cellular networks," *IEEE Trans. Commun.*, vol. 65, no. 9, pp. 3780–3793, Sep. 2017.

[17] M. Alnakhli, S. Anand, and R. Chandramouli, "Joint spectrum and energy efficiency in device to device communication enabled wireless networks," *IEEE Trans. Cognit. Commun. Netw.*, vol. 3, no. 2, pp. 217–225, Jun. 2017.

[18] H. Hu, H. Zhang, and Y.-C. Liang, "On the spectrum- and energy-efficiency tradeoff in cognitive radio networks," *IEEE Trans. Commun.*, vol. 64, no. 2, pp. 490–501, Feb. 2016.

[19] Z. Zhou, M. Dong, K. Ota, J. Wu, and T. Sato, "Energy efficiency and spectral efficiency tradeoff in device-to-device (D2D) communications," *IEEE Wireless Commun. Lett.*, vol. 3, no. 5, pp. 485–488, Oct. 2014.

[20] X. Ge, H. Jia, Y. Zhong, Y. Xiao, Y. Li, and B. Vucetic, "Energy efficient optimization of wireless-powered 5G full duplex cellular networks: A mean field game approach," *IEEE Trans. Green Commun. Netw.*, vol. 3, no. 2, pp. 455–467, Jun. 2019.

[21] P. Goswami, A. Mukherjee, R. Hazra, L. Yang, U. Ghosh, Y. Qi, and H. Wang, "AI based energy efficient routing protocol for intelligent transportation system," *IEEE Trans. Intell. Transp. Syst.*, vol. 23, no. 2, pp. 1670–1679, Feb. 2022.

[22] T. Huang, W. Yang, J. Wu, J. Ma, X. Zhang, and D. Zhang, "A survey on green 6G network: Architecture and technologies," *IEEE Access*, vol. 7, pp. 175758–175768, 2019.

[23] M. Chen, U. Challita, W. Saad, C. Yin, and M. Debbah, "Artificial neural networks-based machine learning for wireless networks: A tutorial," *IEEE Commun. Surveys Tuts.*, vol. 21, no. 4, pp. 3039–3071, 4th Quart., 2019.

[24] P. Annamalai, J. Bapat, and D. Das, "Resource allocation algorithm for hybrid IBFD cellular networks for 5G and beyond," *IEEE Trans. Wireless Commun.*, vol. 21, no. 4, pp. 2414–2429, Apr. 2022.

[25] M. M. Mowla, I. Ahmad, D. Habibi, and Q. V. Phung, "A green communication model for 5G systems," *IEEE Trans. Green Commun. Netw.*, vol. 1, no. 3, pp. 264–280, Sep. 2017.

[26] J. Shi, W. Yu, Q. Ni, W. Liang, Z. Li, and P. Xiao, "Energy efficient resource allocation in hybrid non-orthogonal multiple access systems," *IEEE Trans. Commun.*, vol. 67, no. 5, pp. 3496–3511, May 2019.

[27] D. Zhai, M. Sheng, X. Wang, Z. Sun, C. Xu, and J. Li, "Energy-saving resource management for D2D and cellular coexisting networks enhanced by hybrid multiple access technologies," *IEEE Trans. Wireless Commun.*, vol. 16, no. 4, pp. 2678–2692, Apr. 2017.

[28] F. Fang, J. Cheng, and Z. Ding, "Joint energy efficient subchannel and power optimization for a downlink NOMA heterogeneous network," *IEEE Trans. Veh. Technol.*, vol. 68, no. 2, pp. 1351–1364, Feb. 2019.

[29] K. Hamedani, L. Liu, and Y. Yi, "Energy efficient MIMO-OFDM spectrum sensing using deep stacked spiking delayed feedback reservoir computing," *IEEE Trans. Green Commun. Netw.*, vol. 5, no. 1, pp. 484–496, Mar. 2021.

[30] Y. Guo, C. Skouroumounis, and I. Krikidis, "Joint information and energy transfer of SWIPT-enabled mobile users in wireless networks," *IEEE Trans. Green Commun. Netw.*, vol. 6, no. 2, pp. 1141–1156, Jun. 2022.

[31] J. Wu and W. Chen, "Low-latency and energy-efficient wireless communications with energy harvesting," *IEEE Trans. Wireless Commun.*, vol. 21, no. 2, pp. 1244–1256, Feb. 2022.

[32] P. Yan, Y. Zou, X. Ding, and J. Zhu, "Energy-aware relay selection improves security-reliability tradeoff in energy harvesting cooperative cognitive radio systems," *IEEE Trans. Veh. Technol.*, vol. 69, no. 5, pp. 5115–5128, May 2020.

[33] M. Feng, S. Mao, and T. Jiang, "BOOST: Base station on-off switching strategy for green massive MIMO HetNets," *IEEE Trans. Wireless Commun.*, vol. 16, no. 11, pp. 7319–7332, Nov. 2017.

[34] A. Shahid, V. Maglogiannis, I. Ahmed, K. S. Kim, E. De Poorter, and I. Moerman, "Energy-efficient resource allocation for ultra-dense licensed and unlicensed dual-access small cell networks," *IEEE Trans. Mobile Comput.*, vol. 20, no. 3, pp. 983–1000, Mar. 2021.

[35] M. A. Qureshi and C. Tekin, "Fast learning for dynamic resource allocation in AI-enabled radio networks," *IEEE Trans. Cognit. Commun. Netw.*, vol. 6, no. 1, pp. 95–110, Mar. 2020.

[36] I. AlQerm and B. Shihada, "Energy efficient traffic offloading in multi-tier heterogeneous 5G networks using intuitive online reinforcement learning," *IEEE Trans. Green Commun. Netw.*, vol. 3, no. 3, pp. 691–702, Sep. 2019.

[37] N. Hu, Z. Tian, X. Du, and M. Guizani, "An energy-efficient in-network computing paradigm for 6G," *IEEE Trans. Green Commun. Netw.*, vol. 5, no. 4, pp. 1722–1733, Dec. 2021.

[38] C. Yang, J. Li, Q. Ni, A. Anpalagan, and M. Guizani, "Interference-aware energy efficiency maximization in 5G ultra-dense networks," *IEEE Trans. Commun.*, vol. 65, no. 2, pp. 728–739, Feb. 2017.

[39] Q.-V. Pham, S. Mirjalili, N. Kumar, M. Alazab, and W.-J. Hwang, "Whale optimization algorithm with applications to resource allocation in wireless networks," *IEEE Trans. Veh. Technol.*, vol. 69, no. 4, pp. 4285–4297, Apr. 2020.

[40] C. He, Y. Zhou, G. Qian, X. Li, and D. Feng, "Energy efficient power allocation based on machine learning generated clusters for distributed antenna systems," *IEEE Access*, vol. 7, pp. 59575–59584, 2019.

[41] M. Yan, B. Chen, G. Feng, and S. Qin, "Federated cooperation and augmentation for power allocation in decentralized wireless networks," *IEEE Access*, vol. 8, pp. 48088–48100, 2020.

[42] H. Q. Ngo, L.-N. Tran, T. Q. Duong, M. Matthaiou, and E. G. Larsson, "On the total energy efficiency of cell-free massive MIMO," *IEEE Trans. Green Commun. Netw.*, vol. 2, no. 1, pp. 25–39, Mar. 2018.

[43] M. Rahman, M. Yuksel, and T. Quint, "A game-theoretic framework to regulate freeriding in inter-provider spectrum sharing," *IEEE Trans. Wireless Commun.*, vol. 20, no. 6, pp. 3941–3957, Jun. 2021.

[44] J. Friedrich, S. Frohn, S. Gübner, and C. Lindemann, "Understanding IEEE 802.11n multi-hop communication in wireless networks," in *Proc. Int. Symp. Model. Optim. Mobile, Ad Hoc, Wireless Netw.*, May 2011, pp. 321–326.

[45] M. Saad, "On optimal spectrum-efficient routing in TDMA and FDMA multihop wireless networks," *Comput. Commun.*, vol. 35, no. 5, pp. 628–636, Mar. 2012.

[46] S. Jeon, D. Kim, J. Ahn, R. Ha, and H. Cha, "Revisiting the battery level indicator of mobile devices," *Design Autom. Embedded Syst.*, vol. 25, no. 1, pp. 65–85, Feb. 2021.

[47] D. Ferreira, A. K. Dey, and V. Kostakos, "Understanding human-smartphone concerns: A study of battery life," in *Proc. 9th Int. Conf. Pervasive Comput.*, 2021, pp. 19–33.

[48] D. Chen, M. Haenggi, and J. N. Laneman, "Distributed spectrum-efficient routing algorithms in wireless networks," *IEEE Trans. Wireless Commun.*, vol. 7, no. 12, pp. 5297–5305, Dec. 2008.

[49] M. Saad, "Optimal spectrum-efficient routing in multihop wireless networks," *IEEE Trans. Wireless Commun.*, vol. 8, no. 12, pp. 5822–5826, Dec. 2009.

[50] J. P. Singh, "Development trends in the sensor technology: A new BCG matrix analysis as a potential tool of technology selection for a sensor suite," *IEEE Sensors J.*, vol. 4, no. 5, pp. 664–669, Oct. 2004.

[51] J. Zeng, Z. He, J. Sun, B. Adebisi, H. Gacanin, G. Gui, and F. Adachi, "Deep transfer learning for 5G massive MIMO downlink CSI feedback," in *Proc. IEEE Wireless Commun. Netw. Conf. (WCNC)*, Mar. 2021, pp. 1–5.

[52] Y. Yang, F. Gao, Z. Zhong, B. Ai, and A. Alkhateeb, "Deep transfer learning-based downlink channel prediction for FDD massive MIMO systems," *IEEE Trans. Commun.*, vol. 68, no. 12, pp. 7485–7497, Dec. 2020.

[53] M. Kirişci, "New cosine similarity and distance measures for fermatean fuzzy sets and TOPSIS approach," *Knowl. Inf. Syst.*, vol. 65, no. 2, pp. 855–868, Feb. 2023.
[54] Z. Hongmei, Y. Hailong, and G. Shuting, "Research on path loss and shadow fading of ultra wideband simulation channel," *Int. J. Distrib. Sensor Netw.*, vol. 12, no. 12, Dec. 2016, Art. no. 155014771667984.
[55] Z. Chen and Q. Liang, "Power allocation in 5G wireless communication," *IEEE Access*, vol. 7, pp. 60785–60792, 2019.
[56] M.-T. Nguyen, J. Song, S. Kwon, and S. Kim, "Power allocation for adaptive-connectivity wireless networks under imperfect CSI," *IEEE Trans. Commun.*, vol. 71, no. 7, pp. 4328–4343, Jul. 2023.

VIVEK PATHAK received the B.Tech. degree from Uttar Pradesh Technical University, Lucknow, India, and the M.Tech. degree from the Department of Electronics and Communication Engineering, Visvesvaraya National Institute of Technology Nagpur, Maharashtra, India. He is currently pursuing the Ph.D. degree with the Electrical, Electronics, and Communication Engineering (EECE) Department, Indian Institute of Technology Dharwad, India. His research interests include 6G wireless communication networks, optimization theory and algorithms in wireless communication, machine learning, deep learning, and game theory applications in wireless communication.

R. CHETHAN received the B.Tech. degree in electronics and communication from the PES Institute of Technology, Bengaluru. He is currently pursuing the M.Tech. degree in signal processing and communications with the Electrical Engineering Department, Indian Institute of Technology Kanpur, India. His research interests include wireless communications, machine learning for wireless communications, rate-splitting multiple access, IRS communication, and optimization theory.

RAHUL JASHVANTBHAI PANDYA (Senior Member, IEEE) received the M.Tech. degree from the Electrical Engineering Department, Indian Institute of Technology Delhi, New Delhi, in 2010, and the Ph.D. degree from the Bharti School of Telecommunication, Indian Institute of Technology Delhi, in 2014. He was a Senior Network Design Engineer in the optical networking industry with Infinera Pvt. Ltd., Bengaluru, from 2014 to 2018. Later, from 2018 to 2020, he was an Assistant Professor with the ECE Department, National Institute of Technology, Warangal. Currently, he is with the Electrical, Electronics, and Communication Engineering (EECE) Department, Indian Institute of Technology Dharwad. His research interests include wireless communication, optical communication, optical networks, computer networks, machine learning, and artificial intelligence. He is also working on multiple projects, such as SERB, SPARC, SGNF, and RSM.

SRIDHAR IYER (Senior Member, IEEE) received the M.S. degree in electrical engineering from NMSU, USA, in 2008, and the Ph.D. degree from Delhi University, India, in 2017. He received the Young Scientist Award from the DST/SERB, Government of India, in 2013, and the "Protsahan Award" from IEEE ComSoc, Bangalore Chapter (2020–2021) and (2021-2022). Currently, he is a Professor with KLE Technological University Dr. MSSCET, Belagavi, Karnataka, India. His research interests include semantic communications and spectrum enhancement techniques for intelligent wireless networks.

VIMAL BHATIA (Senior Member, IEEE) received the Ph.D. degree from the Institute for Digital Communications, The University of Edinburgh, Edinburgh, U.K., in 2005. He is currently a Professor with Indian Institute of Technology (IIT) Indore, India, and an Adjunct Faculty Member of IIT Delhi and IIIT Delhi, India. During the Ph.D. degree, he also received the IEE Fellowship for collaborative research with the Department of Systems and Computer Engineering, Carleton University, Canada, and is a Young Faculty Research Fellow from MeitY, Government of India. He has worked with various IT companies for over 11 years, both in India and the U.K. He is a P.I./co-PI/coordinator for external projects with funding of over USD 20 million from MeitY, DST, UKIERI, MoE, AKA, IUSSTF, and KPMG. He has more than 380 peer-reviewed publications and has filed 13 patents (with five granted). He has supervised 20 awarded Ph.D. thesis and two Ph.D. thesis submitted. His research interests include communications, non-Gaussian non-parametric signal processing, and machine/deep learning with applications to communications and photonics. He is an IEEE, Elsevier, Wiley, Springer, and IET reviewer. He is a fellow of IETE and OSI and a certified SCRUM Master. He was a recipient of the Prof SVC Aiya Memorial Award, in 2019. He was also the General Co-Chair of IEEE ANTS 2018 and the General Vice-Chair of IEEE ANTS 2017. He was the Founder and the Head of the Center for Innovation and Entrepreneurship, the Associate Dean of Research and Development, and the Dean of Academic Affairs. He has delivered many talks and tutorials, conducted faculty development programs for the World Bank's NPIU TEQIP-III, and was invited to talk at WWRF46-Paris. He is also an Associate Editor of *IETE Technical Review*, *Frontiers in Communications and Networks*, *Frontiers in Signal Processing*, IEEE Wireless Communications Letters, and IEEE Transactions on Green Communications and Networking. He is currently the DRISHTI CPS Chair Professor with IIT Indore. He is a current member of the Steering Committee of IEEE ANTS. He has been mentioned among the World's Top 2% Scientists by Stanford University.